RI 9395

REPORT OF INVESTIGATIONS/1992

Accuracy and Precision of Microseismic Event Locations in Rock Burst Research Studies

By P. L. Swanson, L. H. Estey, F. M. Boler, and S. Billington

UNITED STATES DEPARTMENT OF THE INTERIOR

BUREAU OF MINES

Report of Investigations 9395

Accuracy and Precision of Microseismic Event Locations in Rock Burst Research Studies

By P. L. Swanson, L. H. Estey, F. M. Boler, and S. Billington

UNITED STATES DEPARTMENT OF THE INTERIOR
Manuel Lujan, Jr., Secretary

BUREAU OF MINES
T S Ary, Director

Library of Congress Cataloging in Publication Data:

Accuracy and precision of microseismic event locations in Rock Burst research studies / by P.L. Swanson . . . [et al.]

p. cm. — (Report of investigations; 9395)

Includes bibliographical references (p. 31).

Supt. of Docs. no.: I 28.23:9395.

1. Rock bursts. 2. Microseisms. I. Swanson, P. L. (Peter L.) II. Series: Report of investigations (United States. Bureau of Mines); 9395.

TN23.U43 [TN317] 622 s—dc20 [622'.28] 91-23343 CIP

CONTENTS

ILLUSTRATIONS

ILLUSTRATIONS—Continued

TABLES

UNIT OF MEASURE ABBREVIATIONS USED IN THIS REPORT

cm	centimeter	m	meter
dB	decibel	m/s	meter per second
ft	foot	μs	microsecond
ft/s	foot per second	ms	millisecond
kHz	kilohertz	mV/g	millivolt per acceleration
km	kilometer	s	second
km/s	kilometer per second		

ACCURACY AND PRECISION OF MICROSEISMIC EVENT LOCATIONS IN ROCK BURST RESEARCH STUDIES

By P. L. Swanson,[1] L. H. Estey,[1] F. M. Boler,[1] and S. Billington[1]

ABSTRACT

Stability analyses of fractured and faulted rock masses require delineation of the position, extent, and orientation of geologic discontinuities. The size of the smallest active discontinuity that may potentially be resolved using the spatial distribution of microseismic event locations is limited by the accuracy and precision of the location methods. At a hard-rock mine in the Coeur D'Alene mining district of northern Idaho, two data sets consisting of calibration blast signals from a known source site and origin time and microseismic event signals were recorded using a stope-wide accelerometer array. These seismic signals are used to quantify various sources of error in event location. Five factors influencing source location errors are examined in this U.S. Bureau of Mines study: (1) biases of the numerical source location techniques, (2) receiver array geometries, (3) uncertainties in receiver positions, (4) errors in picking arrival times, and (5) uncertainties in seismic velocity structure, including the effect of mine openings. In addition, synthetic data (accelerometer positions, travel-time picks and wave velocity) are used to determine the effect of known systematic and random errors on source location calculations. It is shown that the commonly accepted association of minimum travel-time residuals with the best location solution does not necessarily hold true when there is a systematic error in seismic velocity. Recommendations are made for increasing the accuracy and precision of locations of microseismic events detected under similar field conditions.

[1]Geophysicist, Denver Research Center, U.S. Bureau of Mines, Denver, CO.

INTRODUCTION

Deformation in fractured and faulted hard rock is accommodated to some degree by normal and shear displacements along discontinuity interfaces. A deterministic approach to characterizing the mechanics of discontinuous geologic structures requires (1) specification of the locations of major fractures and faults, (2) characterization of their interface (constitutive) properties, (3) specification of the discontinuity-interface and other boundary conditions, and (4) a numerical method for solving specific problems. As part of its effort to gain insight into how mechanical instabilities develop in underground mines and result in rock bursts, the U.S. Bureau of Mines is developing such methods for quantitative characterization of discontinuous rock masses (*1*).[2] The ability to predict the mechanical response of discontinuous rock masses to stress, whether originating in gravity, tectonic, thermal, residual, or applied-induced forces (e.g., mining), is of fundamental importance to scientists and engineers involved in a wide variety of disciplines.

This report addresses one aspect of the mechanics characterization problem, namely that of locating geological discontinuities in areas that are not directly accessible for visual examination. Visual observations made from within mine openings can provide much direct information on the locations of significant discontinuity structures. However, preexisting fractures and faults often terminate abruptly and generally cannot be extrapolated beyond mine openings with a high degree of confidence. This is particularly true in the complex geology of the Coeur d'Alene mining district of northern Idaho where ubiquitous discontinuity structures are observed over a wide range in size scales. In addition, mere visual detection of a fracture or fault does not necessarily provide any information on the influence of the discontinuity on the response of the mine rock to mining-induced stress.

One method, which has the potential to overcome some of these problems, is the use of three-dimensional plots of microseismic event locations in mapping active movements along fractures and faults. An example of a significant fault structure that appears to be delineated by the spatial distribution of microseismicity is shown in figure 1. To adequately resolve similar and smaller discontinuities using this method, it is necessary to locate microseismic events accurately and with high precision. The magnitude of the typical location error sets a lower limit to the dimensions of structures that can be resolved using spatial distributions of microseismic activity. For mine-stability analyses related to rock bursting, the uncertainty in event location coordinates should be less than the smallest mine and geological structures playing important roles in the rock burst process. Accuracy and precision of better than 1 m would be desirable for analyses of small microseismic events in Coeur d'Alene mines.

A variety of receiver array geometries are typically used to study mining-induced seismicity. The arrays range from surface-deployed low-frequency seismic networks to monitor large (local Richter magnitude, M_L, ~5.5) rock bursts occurring throughout a mining district to underground high-frequency arrays with interstation spacing of tens of meters to monitor microseismic events (down to M_L ~-6) in individual stopes (*2*). A single array of several tens of receivers, which is deployed to cover an entire mine, is an intermediate-scale network. Few analyses of errors in seismic event locations from any of these networks have been published. In certain applications, such as the Bureau's rock burst research, this issue is critical.

The motivation for this study stems from observations (*3*) made during the first underground test of a computer-automated-measurement-and-control (CAMAC) digital microseismic data acquisition system (*1*). In this test, attempts were made to compare the locations of 256 microseismic events with known geologic structures. The test site geologic structures are typical of Coeur d'Alene mines. As an example from the test area, figure 2 shows two faults (among others) intersecting near mine openings, possibly forming key block structures (*4*). Accelerometer

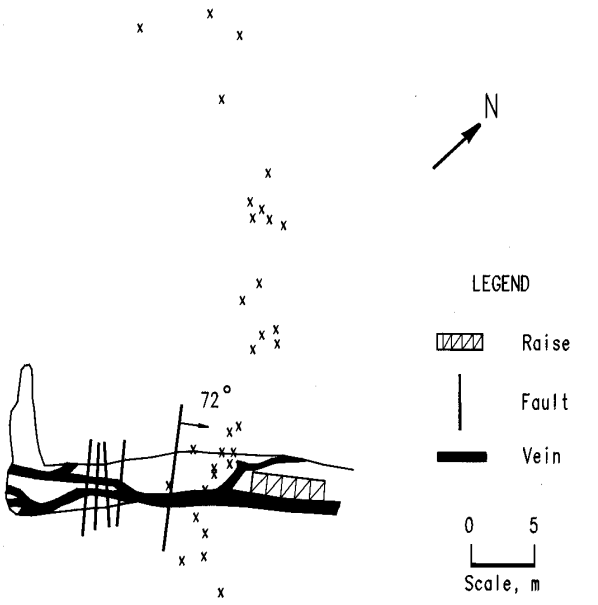

Figure 1.–Spatial distribution of microseismic events (X) delineating a significant and actively adjusting fault (plan view). Microseismic events occurred in response to nearby mining activity.

[2]Italic numbers in parentheses refer to items in the list of references preceding the appendixes at the end of this report.

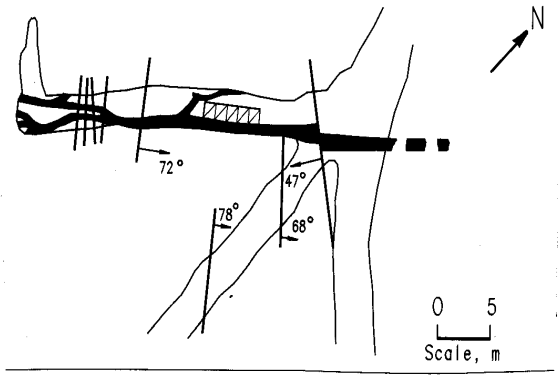

Figure 2.—Block structures formed by intersection of faults with other discontinuities and mine openings (plan view).

waveforms from microseismic activity were recorded in this area and analyzed in terms of first-motion polarity patterns for estimating rupture orientations and slip directions (*3*). The consistency of first-motion patterns indicated that slip was taking place along preferred planes and that the preferred slip directions changed with time and nearby blasting. Unfortunately, the boundaries of these and other similar block structures, which must be determined to evaluate the local mine stability, could not be adequately resolved because of systematic and random microseismic event location errors. A primary goal of this report is to illustrate how these location errors arise.

The report is organized in the following fashion. First, the data acquisition and analysis methods for two different microseismic monitoring systems deployed at the field site are described. Second, estimates of the source location accuracy are provided for each system by comparing calculated and measured calibration blast locations. The problem of location accuracy is further illustrated in a comparison of microseismic event locations calculated using data and analysis methods for each system. In the Error Analysis section, several common source location techniques are first examined and then one method is selected which minimizes bias introduced by numerical methods. The method which minimizes the bias is determined by comparing defined synthetic event locations with locations calculated using controlled amounts of error in travel time, receiver position, and seismic velocity. The influence of receiver array geometry on event locations through amplification of measurement errors is then investigated. Next, the actual or estimated errors in accelerometer position, seismic travel time and velocity associated with the two microseismic monitoring systems are used to calculate average source mislocations for each source of error using random distributions of 1,000 synthetic source sites. The composite accuracy and precision of source locations are then estimated for each system using the combined sources of error. Recommendations are made for increasing the location accuracy of microseismic events for similar arrays. This work is directed at improving safety in the mining industry, a primary goal of the Bureau.

ACKNOWLEDGMENTS

The authors thank ASARCO Inc. for their long-standing cooperation with the Bureau in the field experiments at the Galena Mine, Wallace, ID. The considerable expertise and assistance brought to these field experiments by C. D. Sines was essential for their successful completion. J. Coughlin provided the authors with many details of the hardware and software in the analog microseismic monitoring system.

EXPERIMENTAL PROCEDURES

DATA ACQUISITION AND ANALYSIS METHODS

Two stope-level location systems are investigated. The first is an analog system that is in use at the Galena Mine in Wallace, ID, to characterize space-time statistics of microseismicity. After field trials as a single-stope monitoring system (*5*), it is now being expanded to an industrial-scale computer networked mine-wide system (*6-7*). The second system is a research-grade digital system (*8*) deployed in a single stope and used in characterizing deformation mechanics in fractured rockburst-prone ground.

Figure 3 summarizes the general features of each location system. In the analog system, accelerometer positions are estimated from available mine maps. Up to 32 signals from a stope-level accelerometer array are amplified and fed into a hardware unit that determines the relative arrival times of the first detected phases (*5*). This information is then sent via an RS-232 line to a computer in the instrumentation room for event location calculation and display. The Blake (*9*) source location method (BLD) is used with the assumption of a uniform isotropic seismic wave velocity structure.

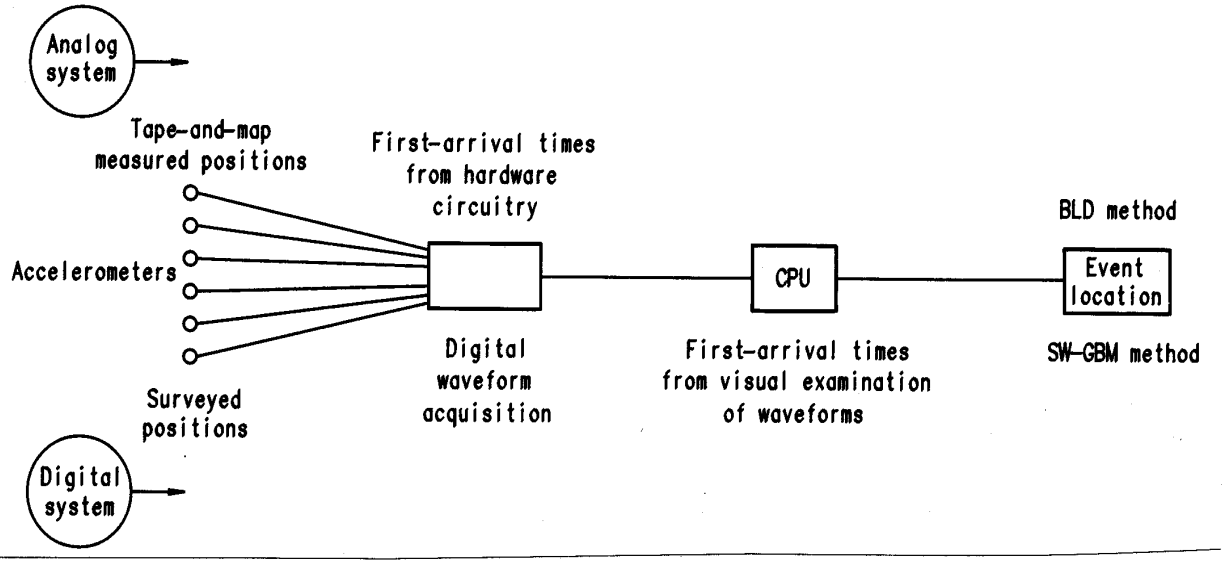

Figure 3.—Main features of analog and digital microseismic monitoring systems. CPU, central processing unit; BLD, Blake; and SW-GBM, Salamon-Wiebols-Godson-Bridges-McKavanagh source location.

In the digital system, data acquisition is based on CAMAC[3] (*8*). Transient accelerometer waveforms from a stope-wide array are captured on up to 32 12-bit analog-to-digital conversion (ADC) channels that are digitized at rates as high as 100 kilosamples per second and transferred via GPIB interface to workstation disk storage. Compressional-wave first-arrival times are determined using a graphics workstation which allows the display of the stored waveforms at any desired magnification. Accelerometer positions are determined using electronic distance-measuring underground surveying techniques where possible. Event locations are calculated using the Salamon-Wiebols-Godson-Bridges-McKavanagh (SW-GBM) method, described later in the report.

ARRAY DESCRIPTION

The set of high-frequency accelerometers from which the arrays for both systems were drawn was distributed in a volume approximately 100 by 100 by 70 m on a side, centered approximately 1.4 km below Earth's surface at the 4300 level of the mine (fig. 4). Thirteen of the receivers (340 mV/g, frequency response up to 5 kHz) were mounted to competent rock surfaces in mine openings with epoxy (rib mounted). An additional 15 accelerometers were mounted triaxially at five locations. Four triaxial borehole probes were installed near the bottom of four NX-size diamond drill holes, 4 m in length. One triaxial unit was rib mounted. Vertical accelerometer coverage was less than ideal, as is typical in a routine monitoring array; all but four accelerometers were located within ±4 m of the 4300 level. Amplifiers close to the accelerometers were used to increase the signal level by a minimum of 40 dB. The amplified signals were brought via cable to an underground instrumentation room 50 m from the center of the array where both the digital and analog data acquisition hardware were located.

CALIBRATION BLAST TESTS

Seismic source location accuracy is often judged by how well the position of a controlled active seismic source, such as a high explosive, can be located. In such tests, it is important to place the sources close to the zone of expected microseismicity, because location accuracy is known to be a function of the array geometry and position within a given array (*10*). A measure of accuracy obtained from controlled source location tests performed under ideal conditions (i.e., source placed in the center of the array,

[3]CAMAC is an international digital interface and modular instrumentation standard (IEEE-583) that readily allows the combination of high-speed transient recorders for acoustic emission, medium-speed transient recorders for microseismic-seismic emission, multiple channels of arbitrary voltage measurement for rock mechanics instrumentation and any other off-the-shelf or custom-designed instrumentation to be interfaced to generic computers through one or more interfaces.

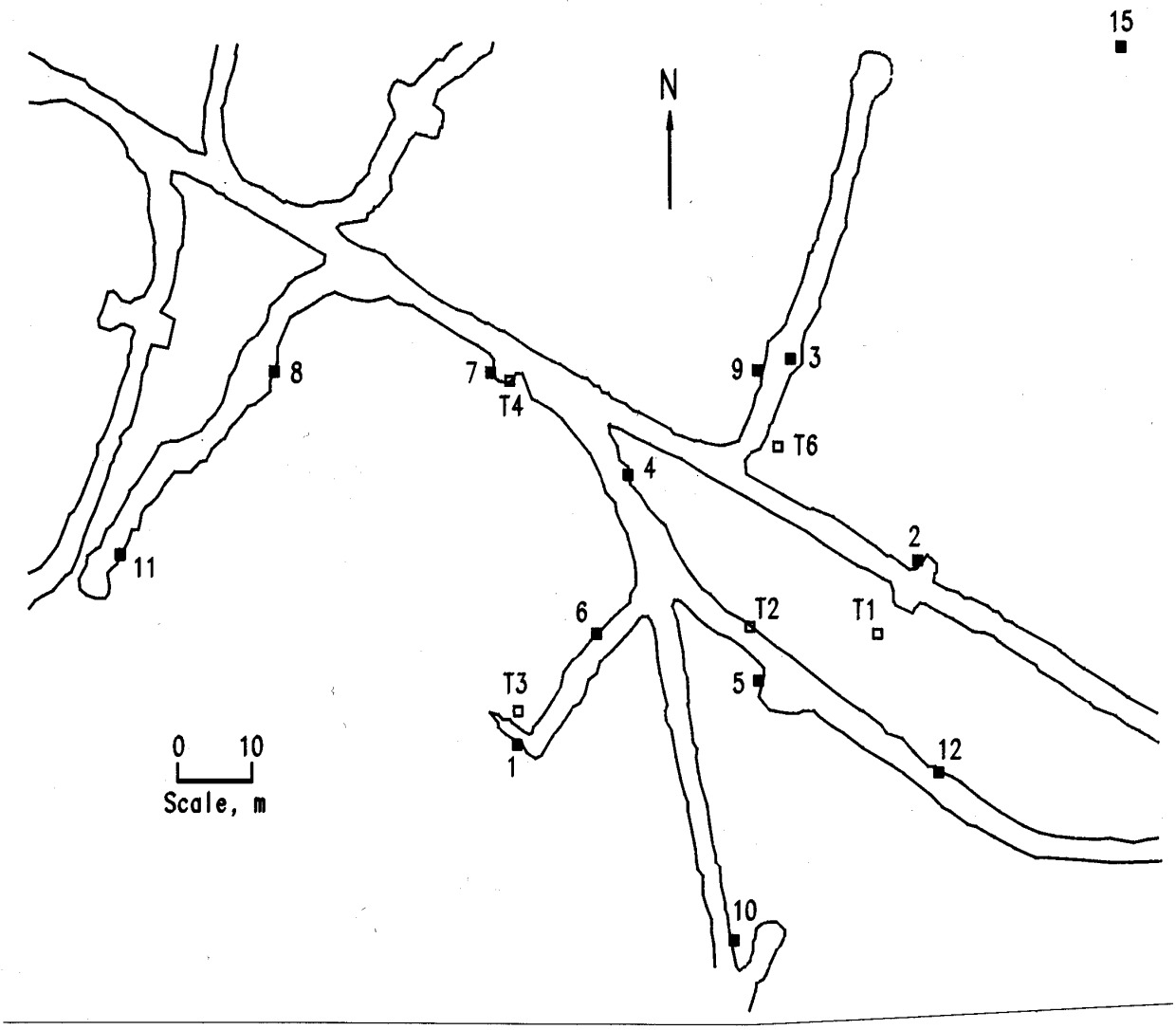

Figure 4.—Plan view of uniaxial (filled squares) and triaxial (open squares) receiver array. Accelerometers 3, 6, 10, and 15 are, respectively, +19, -9, +93, and -53 m above and below the 4300 level.

uniform rock structure, or absence of fracturing and other sources of heterogeneity, abrupt first arrivals, etc.) may not apply at all to microseismic events occurring in a different part of the stope covered by the same array, particularly towards the edge of the array. For this reason, controlled source tests were conducted in the stope toward the bottom edge of the array, approximately 5 m below the main level.

Calibration blasts were made by detonating one-quarter to one-half stick of dynamite placed untamped in a 2-m-long drill hole. With the analog system, the blast waves were detected by the 13 rib-mounted uniaxial accelerometers (fig. 4). Waveforms from both the uniaxial and triaxial accelerometers were recorded with the digital system. An electrical contactor placed in the dynamite with the blasting cap was used as a trigger signal for the digital system. The time history of the trigger signal was recorded and used to determine blast origin time. An example of the blast waveforms and the trigger signal are shown in figure 5.

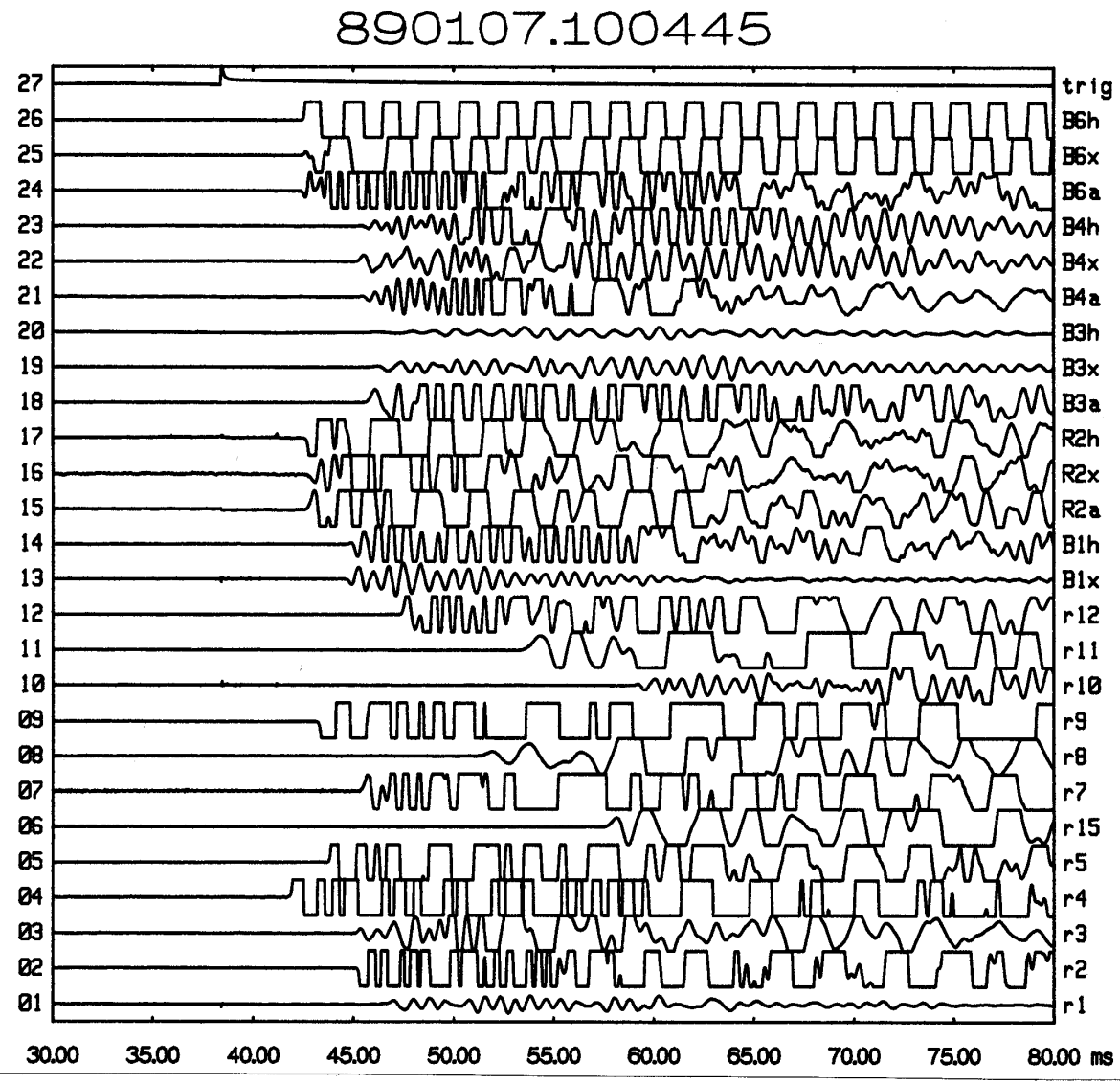

Figure 5.—Example of calibration-blast waveforms and trigger signal (top).

COMPARISON OF SEISMIC SOURCE LOCATIONS

CALIBRATION BLAST TESTS

A series of test blasts was made by repeated detonation in a single drill hole. Figures 6*A* and 6*B* illustrate the calculated blast locations in plan and section views using both the analog (circles) and digital (+) data in comparison to the surveyed blast position (filled triangle).

Two conclusions pertinent to this particular array and site follow from the data presented in figure 6.

1. With either the analog or digital systems, the blast location precision is approximately ±1 m with an accuracy of ±10 m. Average mislocations for analog and digital systems are 10 and 8 m, respectively.

2. The discrepancy between the actual and calculated blast locations is sufficiently small that it does not detract from the demonstrated utility of routine microseismic monitoring using a stope-level array with the present analysis methods. A determination can readily be made when

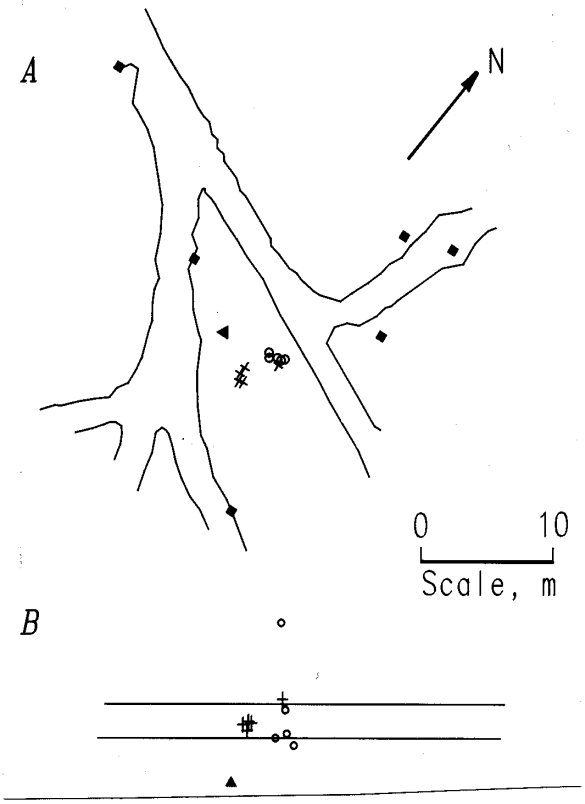

Figure 6.—Comparison between surveyed blast position (filled triangle) and calculated locations using analog system (open circles) and digital system (+ symbols). Diamonds show nearby accelerometer positions. *A*, Plan view; *B*, vertical section in the plane of the vein, looking northwest.

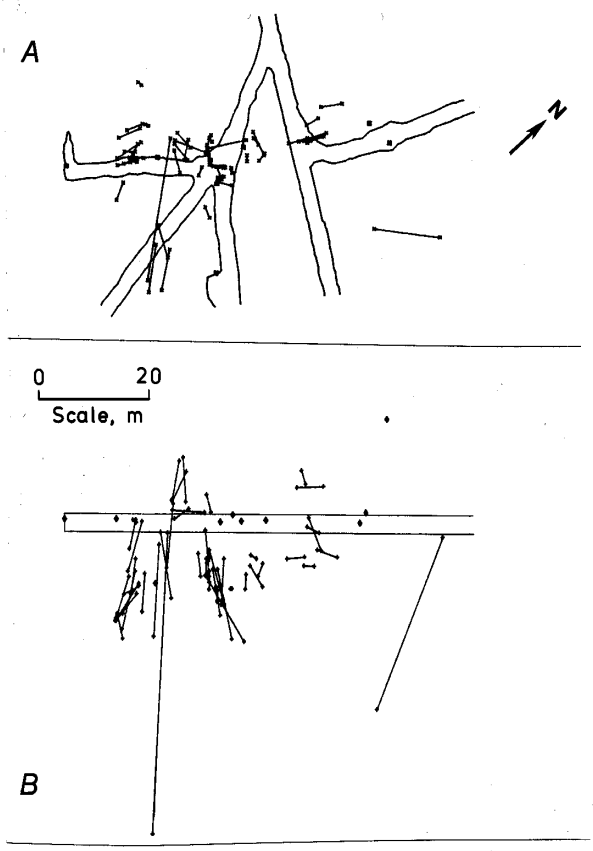

Figure 7.—Comparison of 52 microseismic event locations determined using analog and digital systems. Calculated locations for each event are connected by lines. *A*, Plan view; *B*, vertical section through vein looking northwest.

a particular working area becomes active and approximately where in the area the activity is located. Also, observations of the rates of activity in a given area are not influenced by these location uncertainties. What cannot be determined, in this particular part of the stope, is a precise correlation between microseismic events and a previously identified structural feature, such as a fault, smaller than 10 to 20 m in size. Also, in this part of the array, previously unidentified microseismically active features cannot be spatially defined to an accuracy of better than ±10 m.

MICROSEISMIC MONITORING

The performances of the analog and digital systems were evaluated using microseismic data recorded during a week in which both systems were operating side-by-side. Usually, accelerometer signals were derived from 12 of the uniaxial stations described previously. In the analog system, hardware-determined arrival times are first screened in an attempt to eliminate extraneous picks and picks associated with late-arriving shear waves and/or arrivals from multiple events. Following the calculation of the event location, additional processing ensures that the arrival-time sequence expected on the basis of the calculated location, is consistent with the observed sequence of signal detection; otherwise the event is rejected. During the week of monitoring, the analog system was triggered by 2,070 events, of which 772 were well-located by the criteria just described.

The digital system, using different triggering logic and sensitivity, recorded 266 events. Arrival times at each accelerometer were picked by visual inspection and assigned a quality weighting factor ranging from 0 to 4. Acceptable quality locations for 242 events were obtained. Acceptable quality, in this usage, means that each of the several numerical solution techniques tested (described later) generated locations with relatively low root-mean-square (rms) travel-time residual values. The overlap between the acceptable quality events of the analog and digital systems consisted of 52 events.

A comparison of the locations of these 52 events is shown in plan and vertical section views in figure 7. Most of the 52 event locations for the two systems are different

from each other by less than 4 m in the horizontal plane. The average component of discrepancy shown in the vertical section is significantly larger and is vertically oriented. The average magnitude of the three-dimensional discrepancy vector between the locations is 7.1 m. This figure provides one estimate of the *minimum* uncertainty in the location of microseismic events using these techniques.

The previous comparisons between calculated locations of blasts and microseismic events using the analog and digital systems amply illustrate the need for improvement in location accuracy. The remainder of this report discusses some of the factors which contribute to errors in the calculated locations of calibration blasts and microseismic events.

ERROR ANALYSIS

The following four steps are required for locating seismic sources:

1. Determination of the spatial coordinates (x_i, y_i, z_i) of all transducers in the receiving array.
2. Measurement of the arrival times, t_i, at each station, i, of the compressional wave (or other phase) generated by the transient event.
3. Establishment of an appropriate model of seismic wave velocity, v, structure in the area covered by the array.
4. Solving for the location (x_0, y_0, z_0) and origin time, t_0, using an appropriate technique—numerical or otherwise.

The nonlinear travel-time equation of the seismic signal from the source to the *i*th receiver is

$$0 = [(x_i - x_0)^2 + (y_i - y_0)^2 + (z_i - z_0)^2]^{1/2} - v(t_i - t_0). \quad (1)$$

The velocity field is assumed to be both isotropic and homogeneous, i.e., the signals (either compressional, P, or shear, S, waves) propagate along straight raypaths in all directions at a single value of velocity, v.

It is instructive to quantitatively examine the errors associated with the microseismic source location problem. From equation 1, one of the spatial coordinates of the source can be expressed as

$$x_0 = x_i \pm [v^2(t_i - t_0)^2 - (y_i - y_0)^2 - (z_i - z_0)^2]^{1/2}. \quad (2)$$

By restricting the problem to the one-dimensional case, it can readily be shown how uncertainties in the various known quantities result in errors in the location solution. The one-dimensional analog is

$$x_0 = x_i \pm v(t_i - t_0) . \quad (3)$$

It is customary to obtain an error estimate, δf, of the function $f = f(a, b, c, \ldots)$, which in this case is x_0 above, by

$$\left| \delta f \right| = \left| \frac{\partial f}{\partial a} \delta a \right| + \left| \frac{\partial f}{\partial b} \delta b \right| + \ldots + \left| O(\delta a^2) \right| + \left| O(\delta b^2) \right| + \ldots \quad (4)$$

where the terms on the righthand side of the equation are just the magnitude of the terms of the Taylor series expansion of f. As long as the uncertainties of a, b, c, . . . are small in comparison to a, b, c, the higher order terms can be neglected.

For the one-dimensional location problem, equation 3, the error estimate is

$$|\delta x_0| = |\delta x_i| + |\delta v(t_i - t_0)| + |v \cdot \delta(t_i - t_0)|. \quad (5)$$

Alternatively, the fractional uncertainty in location can be expressed in terms of the source distance, d_i, from the *i*th receiver,

$$\left| \frac{\delta x_0}{d_i} \right| = \left| \frac{\delta x_i}{d_i} \right| + \left| \frac{\delta v}{v} \right| + \left| \frac{\delta(t_i - t_0)}{(t_i - t_0)} \right|, \quad (6)$$

where all the higher order terms are zero since the one-dimensional equation is linear in the quantities x_i, t_i, t_i, and v. Equations 5 and 6 show how uncertainties in measurements of the accelerometer position, δx_i, seismic velocity, δv, and travel time, $\delta(t_i - t_0)$, lead directly to uncertainties in source location, δx_0. This system of one-dimensional linear travel-time equations leads to a coordinate solution with an average uncertainty that is weighted by the measurement uncertainties for each parameter in each equation.

For the two- and three-dimensional cases, the higher order terms of equation 4 generally cannot be ignored, particularly in the presence of significant uncertainties. As measurement errors become large, the dependence of the error in source coordinates (including t_0) on the measurement uncertainties becomes increasingly nonlinear.

In the following sections, the magnitude of each uncertainty term on the right-hand-side of equation 6 is estimated from field measurements for both the analog and digital systems. To examine quantitatively the influence of these measurement errors on three-dimensional locations, several common source location techniques are first examined, and then one method is selected which minimizes bias introduced by numerical methods.

NUMERICAL SOURCE LOCATION TECHNIQUES

Basis Functions

The spatial location (x_0, y_0, z_0) and origin time (t_0) of microseismic events is desired. For sources occurring in a constant velocity medium, equation 1 relates the travel time to the distance between the source and the *i*th receiver. For m arrivals, there are m nonlinear equations that must be solved simultaneously (m linear equations for the one-dimensional case). Since this is difficult to do in a general way, the usual approach is to find some system of linear approximations which can be solved. The term "basis function" or basis will be used to describe the equation actually used in the system of equations to be solved.

For applications typical of the mining environment in which a spatially constant velocity field is assumed, at least two methods have been described (*9*, *11-12*) where the source location can be found directly by solving a system of linear equations, which is obtained after some algebraic manipulation of equation 1. The direct equation developed by Salamon and Wiebols (*11*; which was originally introduced to provide a starting solution for an iterative technique) and Godson (*12*) will be referred to as the SW-GBM basis; that developed by Blake (*9*) will be referred to as the BLD basis. Generalized forms of the basis functions for these two direct methods are given in the appendixes and will be discussed in more detail in a separate publication. Use of these direct solution methods requires special care.

The generalized form of the SW-GBM basis yields m(m-1)/2 different linear equations (equation A-1), since each depends on information from two different receivers (arrival times of the signal and receiver coordinates). From these m(m-1)/2 equations (A-1), many different subsets of m-1 to as many as m(m-1)/2 linearly independent equations can be selected depending upon whether or not weighting is used. The generalized form of the BLD basis yields m(m-1)(m-2)/6 different linear equations (equation A-6) since each depends on information from three different receivers and three different equations can be obtained from each set of three receivers; of these m(m-1)(m-2)/6 equations (A-6), many different subsets of (m-1)(m-2)/2 to as many as m(m-1)(m-2)/6 linearly independent equations can be selected, depending upon whether or not weighting is used. Use of the SW-GBM and BLD bases requires at least five arrivals at different receivers to obtain a meaningful three-dimensional location. At least six arrivals are needed to determine some measure of confidence in the location accuracy. For even modest numbers of receivers, these direct solution methods can result in (1) many linear equations to be solved simultaneously, or (2) some selection of a particular subset of equations out of many different possibilities.

Solving large systems of equations (number of equations $>>$ m) is obviously undesirable. However, if a particular subset of the equations of one of the direct basis functions is used, there is a risk of introducing a bias into the solution. For example, Blake (*9*) considered a particular subset of m-2 equations with the BLD basis, where all m-2 equations of their proposed subset depend on the arrivals at the first and second hit receivers (as well as a third arrival at the other receivers). Errors in the information from the first two stations (i.e., errors in the arrival times and/or receiver coordinates) overinfluence the source solution resulting in unnecessary bias. In a similar fashion, Salamon and Wiebols (*11*) considered a particular subset of m-1 equations with the SW-GBM basis, where all m-1 equations of their proposed subset depend on arrivals from the first hit receiver; this, like Blake's use of the BLD basis, results in a solution overinfluenced by the first hit station. Godson's (*12*) implementation of the SW-GBM basis is considerably better, since all arrivals but two are represented twice, but there is still a slight underrepresentation of information from these two stations. In appendix B, some of the different subsets of the direct basis functions are discussed further.

In general seismological applications, where the velocity field is often known to be heterogeneous (spatially variable) and in some cases anisotropic (directionally variable) and there is considerable incentive to accurately model this velocity field, iterative solution techniques are widely used. The most common approach is to apply some form of the gradient technique (*13*). A Taylor series expansion can be used to find a linear approximation which will be called the gradient basis. The gradient basis is used to form a system of m simultaneous linear equations for m different arrivals at different receivers, where the unknowns are now corrections to some approximate solution which will minimize some function, e.g., equation 1. These corrections, i.e., the gradient of the function being minimized, are then added to the approximate solution to find a new approximate solution. The process is repeated until the correction vector (the gradient) is essentially zero or some other criterion is met. A gradient basis of this type is given in the appendix equation A-8 and determines the source location and origin time; this will be referred to as the full-gradient

basis. Another gradient basis is cast directly only in terms of the source location; the source origin time is incremented separately. This basis will be referred to as the spatial-gradient basis. These types of iterative basis functions are often used in broad application seismological location codes; e.g., a type of full-gradient basis is used in HYPOINVERSE (*14*) whereas a type of spatial-gradient basis is used in HYPO71 (*15*) and HYPOCENTER (*16*). According to Professor M. Salamon, Colorado School of Mines (personal communication), the spatial-gradient basis function solved with an L2-norm minimization is equivalent to the iterative solution method used in Salamon and Wiebols (*11*). Solutions using the spatial-gradient basis function explicitly minimize the sum of the squares of the travel-time residuals with respect to location coordinates and origin time. The constant velocity medium is a special case yielding a simple form for the full-gradient basis equation A-8 and the spatial-gradient basis equation A-9; more complex velocity structures are also amenable to these bases. The gradient bases naturally yield m independent equations, even when weighting is employed.

Solution of Linear Systems

Any of the basis functions previously described can be used, or some variation of them, to form a linear system of equations which can be denoted by the matrix equation $Ax = b$. A is the so-called design matrix, b is the data parameter vector, and x is the unknown parameter vector. Moreover, weighting, which can reflect the measurement uncertainties of the coordinates of each receiver and/or arrival times at each receiver, can easily be incorporated.

There are, of course, many different ways to obtain a solution to the system $Ax = b$. Monte Carlo methods search randomly and other brute force methods search systematically (e.g., G-block, (*9*)) for a solution. Other numerical algorithms allow one to obtain more rigorous estimates of the solution without random or systematic searches.

If the system $Ax = b$ is overdetermined, i.e., the number of equations is greater than the number of unknowns (which is generally the case for microseismic location problems), numerical algorithms such as Choleski's method, QR-decomposition, singular value decomposition (SVD), and linear simplex methods can be used to obtain a solution. An algorithm such as Choleski's method is undesirable since it requires one to set up a new linear problem that has the square of the condition number of the original problem; with this new linear problem (the so-called normal equations), twice as much floating point precision is required to find the solution to the same numerical precision as is possible with the original linear problem (*13, 17-18*).

On the other hand, an algorithm such as SVD is desirable since with it one can get an error estimate for the solution if the measurement errors are normally distributed. This error estimate can either be in the form of a single number representing the uncertainty of each unknown, or in the form of an error ellipsoid which shows how the error is distributed in solution space (*13*). This error estimate is proportional to $|Ax - b|$ (Euclidean L2 norm) and can also be scaled to represent different confidence limits of the uncertainty.

For any set of algorithms, there may be no unique solution x to $Ax = b$, especially when the system is overdetermined. Worse yet, different code—even for the same general type of algorithm (different SVD codes, say)—may give different solutions since there are good ways and bad ways of implementing a numerical algorithm.

Given all of the different possible basis functions (i.e., equations A-1, A-6, A-8, A-9, and others) and all of the different algorithms for solving the system of equations resulting from these bases (and different codes for the same algorithm), what is the best numerical strategy for locating a source? As a result of this investigation, it was discovered that the best strategy seems to depend upon the dominant type of error in the parameters of equation 1.

Numerical Evaluation

The performance of the different combinations of basis functions and linear systems solution algorithms was investigated systematically in the following way. Two different receiver arrays were examined. One was based on an actual array that had been set up to monitor microseismic activity around a specific stope near the 4300 level of the Galena Mine; this was a typical stope array largely concentrated on one mine level with a few receivers located off level. The other was a hypothetical array around an adjacent stope defined using realistic constraints found in the research site (i.e., locations of accessible mine openings, minimum number of borehole sites, etc.) in an attempt to maximize location resolution in all spatial directions inside the array.

A set of 1,000 possible event locations were chosen at random inside a cubic volume 90 m on a side roughly centered on each receiver array and roughly the same size as the array. Two sets of arrival times were calculated. One set was the perfectly known arrival times for these event locations calculated for all receivers assuming a perfectly known constant velocity medium and perfectly known event location and receiver coordinates. Another set of arrival times was produced by adding random errors (using

a pseudo-random number generator) to the perfect arrival times in such a way as to simulate the effects of attenuation and multipathing on the signals received at the receivers, e.g., arrivals at nearby stations were given smaller random error than arrivals at distant stations. To help simulate the effect of changes in receiver subarray geometry, on average 15% of all calculated arrivals were randomly excluded.

Attempts were made to locate the 1,000 synthetic events with each set of arrival times. Attempts included perfectly and imperfectly known values of the velocity and receiver coordinates. Solutions using all four linear basis functions discussed above were examined with a varying number of m receivers. For the BLD basis, the full set of m(m-1)(m-2)/6 equations and various subsets of equations (those suggested by Blake and others subsets discussed in appendix B) were tried, all with and without arrival ordering. For the SW-GBM basis, the full set of m(m-1)/2 equations and various subsets of equations were tried, again, all with and without arrival ordering. For the gradient bases, different starting solutions (e.g., the results of the direct solutions, location of first hit station, geometric center of the array, etc.) were tried.

Several different numerical algorithms for solving the linear systems of equations were tried. The code for the QR algorithm given in Dahlquist and Bjorck (*17*) was rewritten by the second author in the programming language C; the code for the SVD algorithm was adapted from the Fortran code given in Press (*13*); a simplex code was supplied by Riefenberg (*19*). Of these different codes of numerical algorithms, the QR and SVD codes gave essentially the same results (to floating-point accuracy) and both gave more consistent results than the linear simplex code used, since the simplex code was not robust. In principle, however, a robust linear simplex code could give better results than least squares algorithms such as QR or SVD since the resulting solution of a simplex algorithm should be less sensitive to outlying data points (*19-20*).

All of the resulting event locations were examined graphically in three dimensions on an interactive graphics workstation. To present the results in a simple way here, two quantities are tabulated in tables 1 and 2 which apply for both the QR- and SVD-based solution. The first is the average of the magnitude of the difference between the true origin time and the calculated origin time for the 1,000 hypothetical events. The second is the average of the magnitude of the spatial discrepancy vector between the true event location and the calculated location. Table 1 gives the average discrepancy for different amounts of error added to original perfectly known arrival times, receiver coordinates, and/or spatially constant velocity. The results given in tables 1 and 2, and other results summarized below, are based on close to 1,000 different trials of 1,000 synthetic event locations (close to 1 million individual synthetic event locations).

On average, the direct solutions using a SW-GBM basis give smaller discrepancies than the direct solutions using a BLD basis for any type of error. For random errors in arrival time picks or receiver coordinates, the lowest discrepancies of the direct bases tended to be returned by the full independent subsets, followed next by the complete sets of equations. A full independent subset contains only enough independent equations necessary to construct the complete set of equations. Iteration with the gradient bases reduces the discrepancies further; the same average discrepancies for the gradient bases were obtained regardless of the starting solutions that were tried. Also, increasing the arrival time errors by a factor of 4 increases both the temporal and spatial discrepancies of the locations by a factor of close to 4, indicating that the arrival time uncertainties are still small enough to be in the linear realm of equation 4. The arrival time errors were increased by yet another factor of 4 with still a near-linear increase in the total average temporal and spatial discrepancies of the locations. Similarly, increasing the spatial uncertainties of the receivers by a factor of 10 inreases both the temporal and spatial discrepancies of the locations by almost a factor of 10, indicating the larger of the receiver uncertainties are just beginning to affect the solutions in a nonlinear manner.

For random errors in arrival times or receiver coordinates, the gradient bases gave smaller discrepancies than the direct bases.

For systematic errors in the velocity, the results were somewhat different. The smallest location discrepancies were from particular subsets of the direct bases; these subsets of m-1 SW-GBM and m-2 BLD functions used arrival-time ordering and staggered combinations of indices. The largest spatial discrepancies were returned by the gradient bases, though these still yielded very low temporal discrepancies. In fact, although not shown directly in table 1, nearly all solutions based on the spatial- and full-gradient bases tended to give the lowest travel-time residuals. This is a surprising (significant?) result since a minimum in the travel-time residuals is most commonly accepted by seismologists as the solution providing the best location. As indirectly suggested by the temporal discrepancies in table 1, when there is a systematic error in the velocity structure the best location in spatial coordinates is not necessarily provided by the solution with minimum travel-time residuals.

Weighting, if based on reasonable criteria, seems to reduce the location discrepancies, even when only a single parameter is weighted. An explicit numerical example of the event location process is given for each basis function in appendix C.

Table 1.—Performance comparison between numerical source location methods, hypothetical idealized array

Method	Random errors[1]							
	0.000020-s seed		0.000080-s seed		0.10-m seed		1.00-m seed	
	<|dt|>, s	<|dx|>, m	<|dt|>, s	<|dx|>, m	<|dt|>, s	<|dx|>, m	<|dt|>, s	<|dx|>, m
SW-GBM:								
All	0.000048	0.321587	0.000207	1.286343	0.000013	0.100008	0.000118	0.913274
(m-1)SW	.000047	.310034	.000203	1.242515	.000012	.095424	.000112	.871034
(m-1)SW, unordered	.000051	.348318	.000217	1.399101	.000012	.093599	.000113	.888562
mGBM	.000054	.373019	.000227	1.484210	.000015	.111051	.000138	1.046896
mGBM, unordered	.000055	.379864	.000230	1.517062	.000014	.120781	.000127	1.126670
(m-1)GBM	.000054	.374245	.000228	1.491588	.000015	.111640	.000139	1.053041
(m-1)GBM, unordered	.000057	.393101	.000238	1.567563	.000017	.137835	.000152	1.282430
BLD:								
All	.000048	.321577	.000207	1.286334	.000013	.100009	.000118	.913291
FIS	.000047	.310039	.000203	1.242489	.000012	.095408	.000112	.871037
FIS, unordered	.000051	.348302	.000217	1.399082	.000012	.093589	.000113	.888560
(m-2)BLD	.000051	.323467	.000210	1.286971	[3].000883 [.000018	[3]4.573452 .135734]	[3].001038 [.000170	[3]5.768862 1.318323]
(m-2)BLD, unordered	.000071	.490502	.000289	1.946519	.000016	.126929	.000152	1.228279
m, stag[4]	.000080	.633586	.000343	2.658501	.000024	.200586	.000239	1.985059
m, stag[4], unordered	.000064	.456368	.000264	1.833871	.000020	.161289	.000190	1.554032
(m-2)stag[4]	.000070	.506479	.000285	2.029059	.000017	.139757	.000170	1.390946
(m-2)stag[4], unordered	.000069	.496545	.000286	1.996545	.000019	.156417	.000181	1.509601
Spatial gradient	.000033	.232034	.000133	.928197	.000009	.072413	.000092	.724956
Full gradient	.000042	.295770	.000168	1.188689	.000012	.090023	.000123	.897032

	Systematic errors[2]					
	4.8-km/s velocity		5.2-km/s velocity		5.64-km/s velocity	
	<|dt|>, s	<|dx|>, m	<|dt|>, s	<|dx|>, m	<|dt|>, s	<|dx|>, m
SW-GBM:						
All	0.000430	0.443456	0.000395	0.461689	0.001156	1.537918
(m-1)SW	.000410	.775626	.000375	.807509	.001093	2.689754
(m-1)SW, unordered	.000408	.603620	.000373	.628045	.001088	2.092472
mGBM	.000465	.143353	.000429	.149198	.001263	.496736
mGBM, unordered	.000450	.536188	.000413	.558297	.001210	1.859665
(m-1)GBM	.000465	.140838	.000429	.146573	.001263	.488149
(m-1)GBM, unordered	.000451	.543182	.000415	.565731	.001216	1.884122
BLD:						
All	.000430	.443459	.000395	.461698	.001156	1.537929
FIS	.000410	.775622	.000375	.807512	.001093	2.689776
FIS, unordered	.000408	.603640	.000373	.628045	.001088	2.092487
(m-2)BLD	[3].001353 [.000442	[3]5.566338 1.086698]	[3].001245 [.000407	[3]5.602922 1.131223]	[3].001970 [.001197	[3]8.247983 3.768638]
(m-2)BLD, unordered	.000476	.837337	.000438	.871347	.001284	2.902851
m, stag[4]	.000483	1.444480	.000447	1.503387	.001315	5.008366
m, stag[4], unordered	.000485	.630844	.000447	.656648	.001313	2.187363
(m-2)stag[4]	.000475	.073476	.000439	.076661	.001293	.254514
(m-2)stag[4], unordered	.000484	.653189	.000446	.679853	.001309	2.264886
Spatial gradient	.000216	1.866463	.000200	1.827450	.000594	5.673956
Full gradient	.000244	2.022160	.000222	2.043488	.000651	6.577181

	Composite: 0.000020-s seed, 5.2-km/s velocity			
	0.10-m seed		1.00-m seed	
	<|dt|>, s	<|dx|>, m	<|dt|>, s	<|dx|>, m
SW-GBM:				
All	0.000421	0.655878	0.000373	1.254788
(m-1)SW	.000408	.924318	.000368	1.375630
(m-1)SW, unordered	.000408	.784399	.000393	1.379033
mGBM	.000449	.458182	.000394	1.294263
mGBM, unordered	.000441	.766041	.000406	1.475807
(m-1)GBM	.000448	.457550	.000394	1.299613
(m-1)GBM, unordered	.000439	.781610	.000383	1.579993
BLD:				
All	.000421	.655882	.000372	1.254773
FIS	.000408	.924340	.000368	1.375599
FIS, unordered	.000408	.784390	.000393	1.379038
(m-2)BLD	.000452	1.235036	.000466	1.907337
(m-2)BLD, unordered	.000459	1.072379	.000479	1.868078
m, stag[4]	.000479	1.632003	.000523	2.698924
m, stag[4], unordered	.000484	.918189	.000467	1.851980
(m-2)stag[4]	.000461	.549581	.000454	1.725068
(m-2)stag[4], unordered	.000481	.985816	.000452	1.858796
Spatial gradient	.000234	1.963932	.000231	2.259208
Full gradient	.000257	2.197501	.000237	2.563209

See notes at end of table 2.

Table 2.—Performance comparison between numerical source location methods, 4300-115 array

Method	Random errors[1]						Systematic errors[2]	
	0.000020-s seed		0.10-m seed		1.00-m seed		5.2-km/s velocity	
	<|dt|>, s	<|dx|>, m	<|dt|>, s	<|dx|>, m	<|dt|>, s	<|dx|>, m	<|dt|>, s	<|dx|>, m
SW-GBM:								
All	0.000074	0.636034	0.000011	0.146400	0.000114	1.500710	0.000414	1.436337
(m-1)SW	.000071	.607230	.000010	.142696	.000111	1.462420	.000420	1.843113
mGBM	.000080	.681949	.000013	.156918	.000131	1.600344	.000401	1.001503
(m-1)GBM	.000080	.687508	.000012	.155039	.000129	1.582105	.000409	.913786
BLD:								
All	.000074	.636005	.000011	.146412	.000114	1.500718	.000414	1.436337
FIS	.000071	.607285	.000010	.142737	.000111	1.462448	.000420	1.843138
(m-2)BLD	.000075	.627874	[3].022649	[3]113.42168	[3].005678	[3]29.49322	[3].018368	[3]95.147606
			[.000013	.164976]	[.000131	1.674416]	[.000440	1.837818]
m, stag[4]	.000111	.994049	.000022	.234148	.000220	2.359569	.000410	1.987207
(m-2)stag[4]	.000133	1.222574	.000020	.220254	.000200	2.271821	.000415	.550042
Spatial gradient	.000052	.377889	.000007	.096421	.000076	.969821	.000480	2.166670
Full gradient	.000060	.467821	.000011	.130575	.000116	1.319788	.000495	3.201569

	Composite: 0.000020-s seed, 5.2-km/s velocity			
	0.10-m seed		1.00-m seed	
	<|dt|>, s	<|dx|>, m	<|dt|>, s	<|dx|>, m
SW-GBM:				
All	0.000479	1.866042	0.000512	2.112272
(m-1)SW	.000482	2.238079	.000518	2.391626
mGBM	.000459	1.477663	.000491	1.996528
(m-1)GBM	.000463	1.423559	.000498	1.988969
BLD:				
All	.000479	1.866079	.000512	2.112242
FIS	.000482	2.238074	.000518	2.391557
(m-2)BLD	.000489	2.264748	.000528	2.851486
m, stag[4]	.000490	2.593844	.000559	3.474861
(m-2)stag[4]	.000517	1.818175	.000706	4.175456
Spatial gradient	.000534	2.675963	.000539	2.758379
Full gradient	.000558	3.579921	.000559	3.438499

<|dt|> Mean of absolute differences between synthetic and calculated source origin times.
<|dx|> Mean of absolute differences between synthetic and calculated source locations.
BLD Blake-Leighton-Duvall generalized basis function (see text).
SW-GBM Salamon-Weibols-Godson-Bridges-McKavanagh basis function (see text).
FIS Full independent subset (one possiblity, see text).

[1]0.000020-s seed—largest possible error for stations approximately within 20 m is 0.020 ms, within 20 to 40 m is 0.040 ms, within 40 to 100 m is 0.080 ms, and within 100 to 200 m is 0.160 ms. 0.000080-s seed—4 times the time uncertainty of 0.000020-s seed. 0.10-m seed—largest spatial error of any Cartesian receiver coordinate is 0.10 m. 1.00-m seed—largest spatial error of any Cartesian receiver coordinate is 1.00 m.

[2]4.8- and 5.2-km/s velocity—used for average P velocity rather than 5.0 km/s. 5.64-km/s velocity—5.6388 km/s (18,500 ft/s) used for average P velocity rather than 5.0 km/s.

[3]1 location was mislocated by a very large amount. Bracketed data are averages based on 999 locations (large mislocation removed).

[4]Staggered ordering; that is, triplets 123, 234, 345, . . ., (m-2)(m-1)m (see appendix B).

Summary and Recommendations

When the errors are randomly distributed (such as is the case for most receiver coordinates and for arrival times), a good approach is

1. use one of the direct bases (either SW-GBM or BLD) to form a subset of linear equations (e.g., using one of the subsets suggested in appendix B), solve using a good QR or SVD code, and obtain a first approximate solution for the location;

2. use a gradient basis with this approximate solution to form new system of m linear equations, solve for gradient using QR or SVD code, form new approximate solution, and iterate until gradient is essentially zero or other criterion is met (note: if a minimization of travel-time residuals is desired, use the spatial-gradient basis);

3. if error estimates are desired (assuming that all errors are normally distributed), perform one (or two) more iterations with SVD code and compute confidence regions of the solution.

When the errors are mainly systematic, as in the case of modest deviations of the trial velocity from synthetic known velocity, the best approach may be to use the SW-GBM basis with the staggered subset suggested originally

by Godson (*12*), i.e., m-1 pairs ordered by arrival times. Apparently, by ordering the arrivals and selecting time-ordered pairs, the terms of equation A-1 involving the velocity in the SW-GBM basis are kept at a minimum and, in this way, impact the total solution the least. Moreover, this subset of the SW-GBM basis also does reasonably well when the errors are random. (Note: Even though the m-2 BLD subset of staggered triplets with arrival-time ordering gives better results with only systematic velocity errors, this subset does not perform very well with random errors.)

Thus, if the dominant source of error is random, the iterative gradient bases give the best solution, the spatial gradient basis being slightly better than the full gradient basis. If the dominant source of error is a systematic uncertainty of the velocity, a special subset of the SW-GBM basis functions may give the best solution; this has been selected as the preferred location technique.

For the rest of this report, sources are located using the SW-GBM basis with ordered arrivals (m-1 equations) to get a quantitative assessment of the influence of the measurement errors on event locations.

INFLUENCE OF RECEIVER ARRAY GEOMETRY ON EVENT LOCATION ERRORS

The importance of installing a receiver array that provides thorough coverage of the volume to be monitored is usually appreciated by those monitoring mining-induced seismicity, but difficult to achieve in practice. Receiver positions are typically constrained by available access. Poor array geometries, and/or poor coverage by adequate geometries, can greatly amplify the effect of small measurement errors (e.g., Ge (*10*)) and lead to poorly constrained locations.

A graphical event location technique that illustrates the way in which array geometry affects the sensitivity of event locations to measurement errors has been used by the authors in analyzing the degree of constraint placed on event locations by receiver array geometries (*21*). In an isotropic velocity medium, three-dimensional surfaces of constant relative arrival time, or isochrons, are constructed for each pair of receivers reporting first arrivals (e.g., curve AB for receiver pair AB in figure 8*A*). This three-dimensional hyperboloid surface, which is symmetric about the line connecting the receivers, is a solution to an equation formed by subtracting P-wave arrival times for the receiver pair in question using equation 1. It represents all possible positions of a source that are consistent with the measured difference in P-wave arrival time for the receiver pair. The infinite number of possible solutions for the source location on this surface is reduced by considering additional relative-arrival-time isochron surfaces from other receiver pairs. The mathematical solution for the event location can be graphically interpreted as the common point of intersection of all of the isochron surfaces. In some situations, multiple solutions are possible.

When errors in travel time are added to the exact relative arrival-time data, the isochron surfaces do not intersect at a point, but instead cluster throughout a volume.[4] The size, shape, and orientation of this volume depends not only on the magnitude of the errors but also on the angles of isochron surface intersection; the geometry of the reporting receivers determines these angles. If the errors are normally distributed, the isochron intersection volume is characterized by the SVD error ellipsoid.[5] The lengths of its axes are inversely proportional to the amount of constraint on the solution in that direction and thus provide a visual indication of the influence of array geometry on possible event location errors. If the SVD ellipsoid is equidimensional, the center of the intersection volume (fig. 8*A*) does not significantly change with small adjustments in isochron position due to small measurement errors.[6] However, if the SVD error ellipsoid has one dominant axis (fig. 8*B*), then small measurement errors (e.g., receiver pair AC) can produce large displacements of the intersection point.

Maximum constraint on the solution can be achieved by minimizing measurement errors and selecting an optimum receiver geometry such that the number of isochrons that intersect at small angles is minimized. This is achieved by completely surrounding the events to be located with a three-dimensional distribution of receivers. Linear and planar array geometries for three-dimensional locations

[4]Errors in travel-time pick, velocity along the raypath to the receiver, and the station coordinates all result in uncertainty in the position of a relative-arrival-time isochron.

[5]The various numerical location techniques evaluated in the previous section were concerned with determining which kind of isochron surfaces were to be used in the location process. For a given set of arrival times, each basis function produces slightly different volumes of intersecting solution surfaces. The different numerical solution algorithms (QR, SVD, etc.) define a best location point within these volumes.

[6]Larger errors may completely change the position, shape, and orientation of the error ellipsoid and may also result in nonintersecting isochron surfaces.

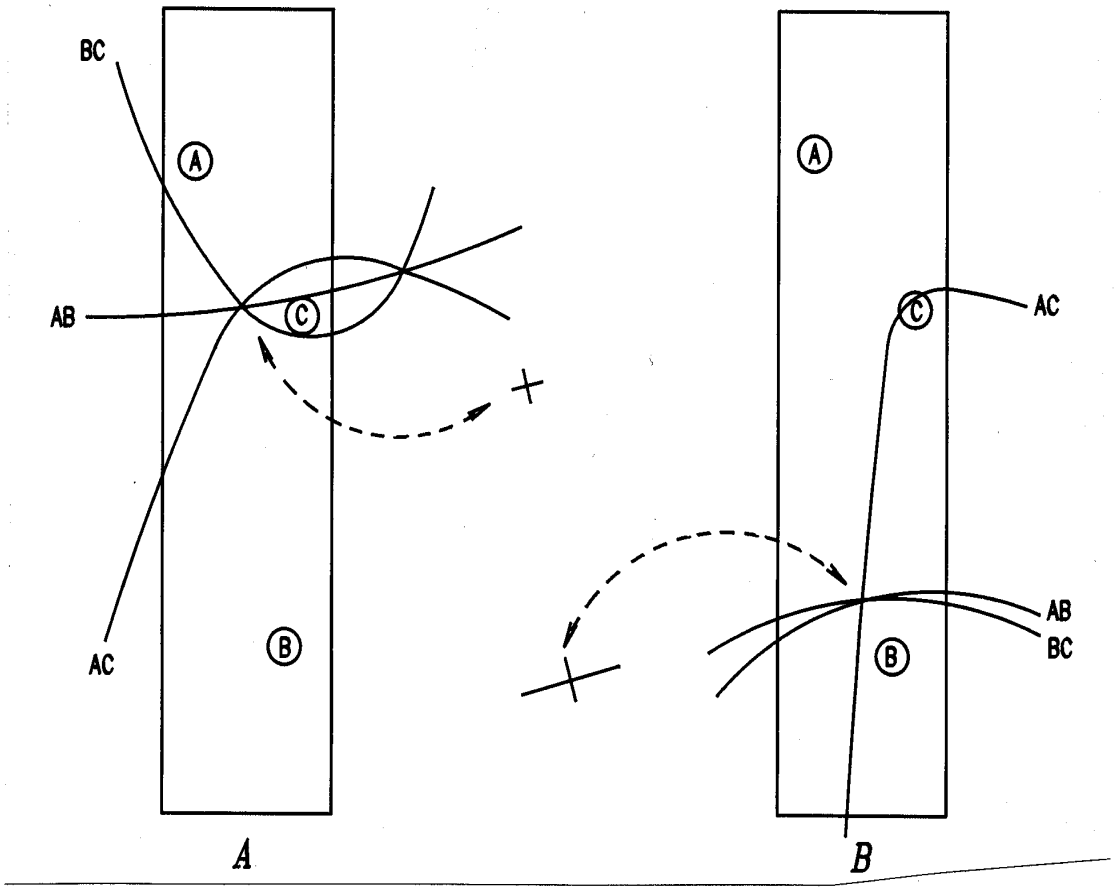

Figure 8.—Seismic event locations using intersections of relative-arrival-time isochrons. A, B, and C are receivers; AB, AC, and BC are receiver pairs. *A*, Well-constrained location with small equidimensional (schematic) SVD error ellipsoid; *B*, poorly constrained location with elongate SVD error ellipsoid axis parallel to direction of least constraint.

are to be avoided. These provide little constraint perpendicular to the axis and/or plane of receivers because the relative arrival-time isochron surfaces largely intersect at very shallow angles for all sources placed off axis or off plane. Slight measurement errors can result in very large displacements of the solution along the long axis of the intersection volume (or SVD ellipsoid; fig. 8*B*).[7]

[7]These array geometries lead to difficulties in three-dimensional location solutions even without errors. For example, two-dimensional (planar) arrays result in a mirroring of the location solution about the symmetry plane and linear arrays lead to an infinite number of solutions along a co-axial circle. Another solution problem arises when stations are distributed on the surface of a right-circular cone with the source at its apex (11).

The effects of linear or planar receiver geometries can be present in an otherwise three-dimensional array when only a subset of the receivers have usable arrivals for the location process. This is especially true for array geometries that are initially biased toward linear or planar receiver distributions. Only the largest events, representing a rather small fraction of all detected events, provide usable signals on all receivers, and thus actually use the full three-dimensional extent of an array.

Since many mining geometries provide access points for receiver installation on a plane (e.g., coal and vein deposits), it is common for underground arrays to possess groups of stations that approximate planar distributions.

Subsets of these receiver stations also tend to take on linear distributions within this plane (e.g., fig. 4) due to restricted access (i.e., drifts, raises, crosscuts, etc.). As the number of receivers reporting usable first arrivals is reduced, due (e.g., to low amplitudes of small magnitude events), the probability of forming a predominantly linear or planar array increases.[8]

Figure 9 illustrates how the constraint on the solution can be influenced by the geometrical distribution of a subset of reporting stations. The overall receiver array is the same as shown in figure 4. Figures 9*A* and 9*B* show two different sets of five receivers which are used in graphical locations of the same event. Similar measurement errors were added to the exact data from each receiver. From the angles of intersection of isochrons near the source location, it is immediately recognizable that there is much more uniform constraint for the receiver distribution in figure 9*A* than in 9*B*.

A comparison of the calculated event locations and their associated SVD error ellipsoids is shown in the figure inserts (lower left-hand corners). As expected from the isochron intersections, the SVD error ellipsoid in figure 9*A* is quite equidimensional compared to figure 9*B*. In both cases, the calculated event location is displaced away from the exact location along the direction of the long ellipsoid axis. The magnitude of the mislocation observed with the linear array subset of figure 9*B* (1.8 m) is approximately 2.5 times that observed with the array subset that surrounds the source in figure 9*A* (0.7 m). This illustrates the strong influence of source and receiver-array geometry on the sensitivity of a location position to measurement errors.

While the array subset in figure 9*A* appears to yield adequate constraint in the horizontal plane, there is no constraint for either array subset in the vertical direction. Thus the mislocations represent an absolute lower bound. The reporting receivers need only *weakly approximate* a linear or planar distribution to form poorly constrained solutions.

[8]This aspect of the effect of array geometry is partly simulated in the error analyses in previous and subsequent sections by randomly excluding 15% of the stations in each simulated-source location calculation for both the analog and digital systems. On average, 7.5 stations were used with the digital system in locating the microseismic events shown in figure 7. Occasionally, only five stations were used (less than 5% of this particular data set). Since first-arrival picking with hardware results in significantly fewer usable signals than with manual waveform picking, the number of reporting stations for the analog system has been overestimated. As a result, the location discrepancies reported for the analog system have been underestimated.

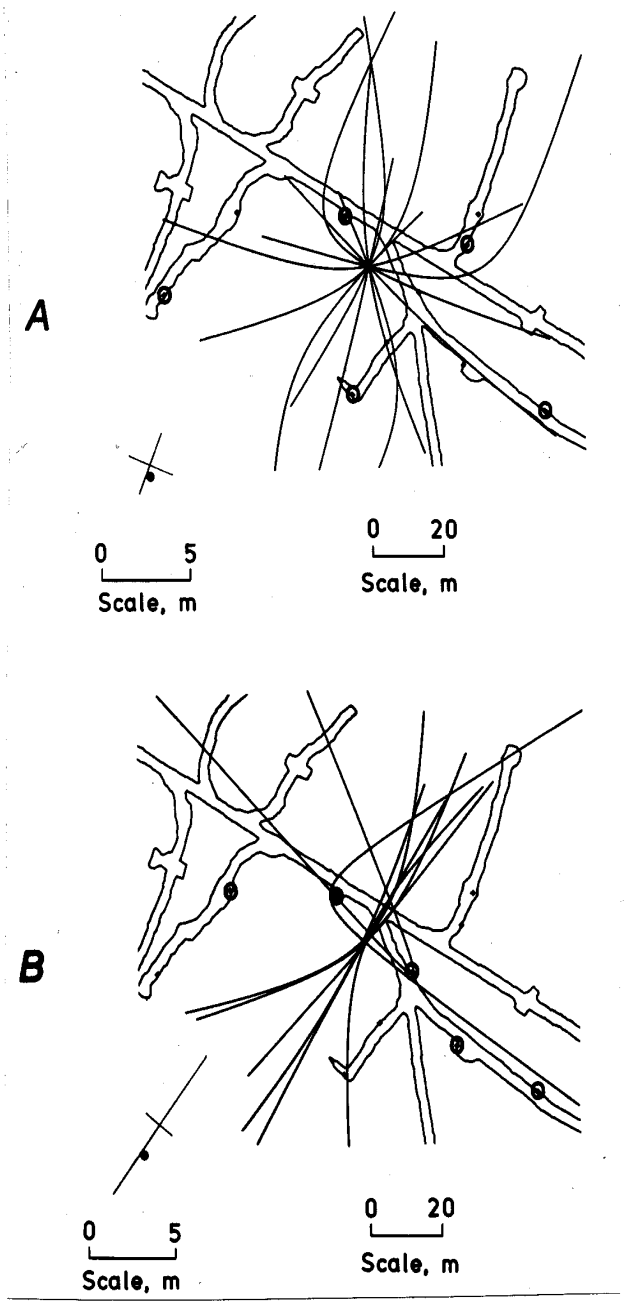

Figure 9.—Influence of receiver array geometry on event location errors. A synthetic source location (open circle in insets) is calculated (center of SVD ellipsoid axes) using small amounts of error added to exact travel-time data for two different arrangements of five (circled) receivers. Relative-arrival-time isochrons are shown for comparison. *A*, Uniform receiver coverage yields uniform isochron intersections and equidimensional SVD error ellipsoid; *B*, quasi-linear array yields large elongate error ellipsoid and larger mislocation for equivalent measurement errors.

ACCELEROMETER POSITION MEASUREMENT

To describe the positions of receivers and microseismic sources, a frame of reference is needed. Mines often establish survey control points on a system of east and north and elevation coordinates, and produce drift outline maps as workings proceed. Drift outline maps show the plan view relative to east and north grid lines at one horizontal level or in vertical section. The accuracies of such maps vary tremendously depending upon the intended application. In the study area, the mine survey and drift maps were established approximately 30 years ago. As this area has been subjected to continual deformation associated with vertical stope mining under high horizontal stress (sandfilled stope closures as great as 0.5 m (22)), including rib sloughage and rock burst deformation, the relative positions of certain survey control points are expected to have changed significantly since the original survey.

Existing (30-year old) mine maps provide the frame of reference for accelerometer positions in the analog system. The usual method is to find a recognizable feature on the map that is close to the accelerometer in question; the distance to the accelerometer from this feature is then measured and plotted on the map. The vertical coordinate is typically referenced to the track or floor level.

Several sources of error are associated with this method. First, the accelerometer cannot be located to better than the accuracy of the original mine map, even with perfect identification of a position on the map. Second, the map representation of a rib (a single line) is only an approximation to a rough three-dimensional surface. Third, changes in mine opening geometry occur with time due to rib sloughage and other mining-induced deformation such as rock bursting. Rock bursting also produces ground deformation in excess of obvious surficial modifications to mine openings. Overall, the uncertainty for the accelerometer position determinations used by the analog system is conservatively estimated at 1 m.

Control points of the 30-year old mine survey provide the frame of reference for accelerometer position determination in the digital system. Two surviving survey control points (most of the survey spads have not survived 30 years of mining activity) were used to establish a baseline to which all calculated accelerometer positions were referenced. The coordinates of one point also serve as the tie-in to the mine coordinate system. Accelerometer positions are established by measuring angles and distances using a theodolite equipped with an electronic (infrared) distance-measuring (EDM) device. Occasionally, in difficult-to-survey or obstructed areas, short distances to accelerometers are estimated using tape, compass, and inclinometer readings.

The overall uncertainty in accelerometer positions using these techniques is estimated to be ±5 cm. This location uncertainty is referenced back to the particular mine survey spads used to establish the reference baseline and not the original mine maps themselves. Thus, systematic discrepancies may exist between the locations of accelerometers plotted on these maps and the locations of mine openings on the map due to systematic errors (1) in the original mine map, (2) from subsequent deformation in the surveyed area including displacement of survey control points, and (3) in the accelerometer survey itself.

Table 3 shows the differences between accelerometer position coordinates determined using the analog and digital systems. Differences in individual station coordinates ranged from 0.02 to 1.9 m (0.07 to 6.21 ft). The average three-dimensional discrepancy vector has a magnitude of approximately 1 m. Systematic differences between the two sets of measurements were minimized by finding a best fit coordinate transformation (rotation and translation) between the two sets of accelerometer coordinates. One is left with an estimate of the quasi-random differences between the two methods shown as residuals in the bottom half of table 3. These differences are representative of both the random measurement errors associated with the two methods of determining accelerometer position and deformation-related displacements occurring since establishing the two reference frames. The individual station coordinate residuals range from 0.02 to 1.43 m (0.08 to 4.7 ft). The average best fit three-dimensional discrepancy vector has a magnitude of 0.79 m (2.6 ft).

Table 3.—Difference between surveyed and tape-and-map-measured accelerometer coordinates before and after transformation, feet

Station	Δx	Δy	Δz	|Δr|
BEFORE				
1	1.82	-0.09	-1.71	2.50
2	-.72	1.42	-.71	1.74
5	-.34	.54	.08	.64
7	2.72	1.96	1.10	3.53
8	-1.43	1.89	-1.73	2.93
9	-5.58	-.78	-.07	5.63
11	1.70	6.21	-1.03	6.52
12	.12	-1.21	-.83	1.47
Average	NAp	NAp	NAp	[1]3.12
AFTER				
1	2.97	-2.16	1.34	3.91
2	.32	.55	-1.11	1.28
5	.08	.81	-.45	.93
7	1.12	1.22	-1.47	2.21
8	-2.43	-.56	1.29	2.81
9	-4.68	-.37	-.30	4.70
11	1.94	3.84	.62	4.35
12	1.49	-1.20	.46	1.97
Average	NAp	NAp	NAp	[2]2.61

NAp Not applicable.
[1]0.95 m.
[2]0.79 m.

The differences in simulated microseismic event locations, caused by position errors of the same magnitude as the differences in the two sets of accelerometer position measurements, are illustrated in figure 10. This figure shows 1,000 defined event locations selected at random in a volume that is typically monitored by an array such as found in figure 4. Exact travel-time data were calculated from the distance between the defined event locations and the surveyed station coordinates using a constant velocity. In figure 10, event locations calculated using these travel-time data and the tape-and-map-measured accelerometer positions are connected with lines to the exact locations.

The interconnecting lines graphically illustrate the spatial variation in location discrepancy; the flow-line trend is generally consistent with the trend of major axes of the calculated SVD error ellipsoids. Of course, the discrepancies become greatest when the event is located outside of the array volume. In most routine monitoring situations, due to the restrictions on where receivers can conveniently be located, many events occur below most, or all, of the receivers in a typical array (i.e., in the active workings of the stope) where constraint in the vertical direction is typically at a minimum.[9] The average magnitude of the three-dimensional discrepancy vector connecting the two locations *in the particular volume* of figure 10 is 2.3 m.

This number is very dependent upon the particular accelerometer array geometry and the particular control volume selected and is thus identified only to assist in making *relative* comparisons of discrepancies calculated using the same array and control volume. The same surveyed accelerometer array and random event volume is used in the next several sections to allow comparison of the three-dimensional location errors resulting from errors in travel time and velocity. For these comparisons, the surveyed station coordinates are considered to be exact.

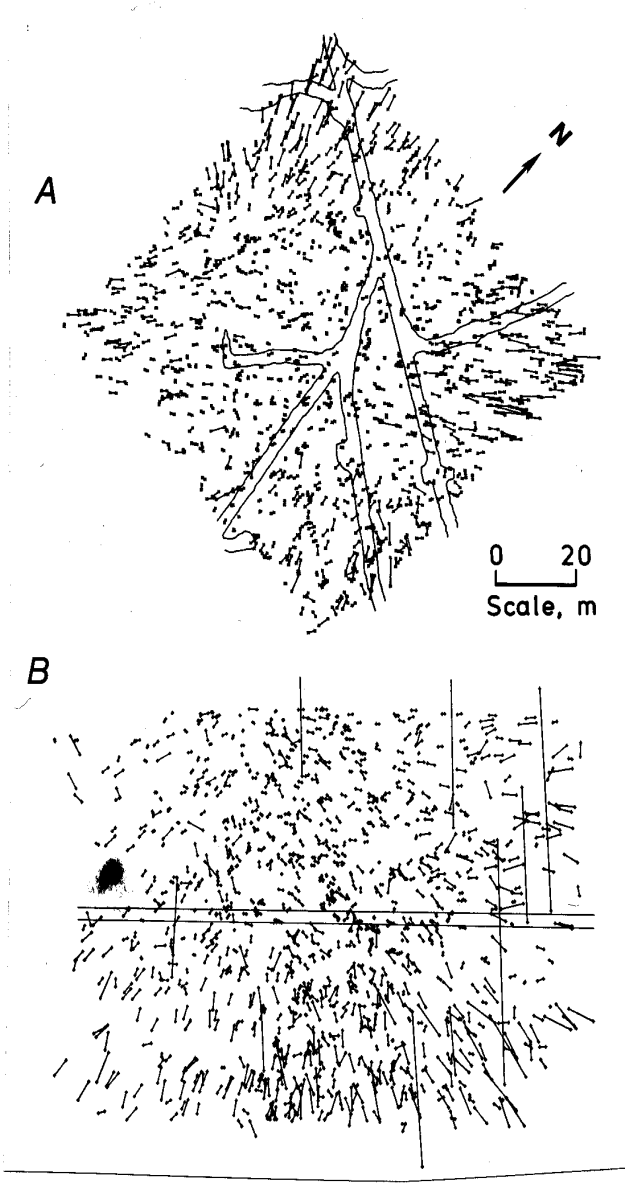

Figure 10.—Defined event locations selected at random in control volume centered on receiver array (from fig. 4) connected with straight lines (flow lines) to event locations calculated with accelerometer position measurement errors. Flow lines indicate directions of least constraint on event location solutions. *A*, Plan view; *B*, vertical section looking northwest.

ARRIVAL TIME DETERMINATION

Arrival time determination methods can be divided into hardware timing (picking), manual timing, and software timing. Each method has advantages and disadvantages. A related topic is the assignment of some sort of quality descriptor to the pick which is used to weight the arrivals in the numerical solution for the location. Weighting is possible, in theory, for all of the above methods.

[9]The several *very* long vertically oriented discrepancy vectors in the vertical section may indicate a mirroring of the solution, or convergence to one of several possible solution sites. In general, such behavior was observed when either increasing the measurement errors or decreasing the number of stations used in the location.

Hardware Timing

Using hardware electronics to examine transient voltage signals at each accelerometer offers the ability to determine arrival times without tedious examination of every

channel for each event. Hardware-determined arrival times are thus suited to near-real-time calculation of event location. Another advantage is that computer mass storage can be conserved. A variety of electronic circuits can be used in hardware timing. The errors in picks can be attributed to both the inherent errors in the electronics and the inability of the hardware to readily handle wide variations in signal shapes and signal-to-noise ratios. A simple voltage threshold exceedance is used for the analog system. For a signal whose onset approximates a step function, this method will have an inherent error equal to the time resolution, including channel synchronization, designed into the electronics. This resolution is 100 μs for the analog system (*23*). For signals which are emergent, i.e., which have a relatively long rise time, the time to the threshold exceedance is correspondingly longer, and the pick will be in error by an amount proportional to the rise time. As high frequencies are selectively attenuated with propagation distance (e.g., fig. 5), rise times increase; thus picking errors systematically increase with wave propagation distance. Systematic timing errors also occur at individual receiver stations when they experience low-pass filtering due to poor coupling into the host rock and thus produce emergent signals.

Another common source of error results when the voltage threshold is not exceeded upon receipt of a low-amplitude compressional wave arrival, yet is subsequently exceeded by the shear wave or other later-arriving phase; this is potentially a systematic source of arrival-time error. The magnitude of this error is proportional to the distance to the event and the difference in velocities of the two phases.

Manual Timing

If a permanent record of the signals exists, either on chart paper, in a digitizing oscilloscope memory, or in computer mass storage, manual arrival-time picking from visual examination of the record is possible. (Both manual and software timing offer the advantage of being able to reprocess the data if permanent records are kept.) The errors inherent in this method will correspond to how the signal is stored, the skill and consistency of the person doing the picking, and the quality and shape of the signal. Further discussion of manual picking will be restricted to the case of computer mass storage of digitized signals, which can then be displayed at any desired magnification. Assuming no other errors in the data acquisition and display electronics, the digitization interval will be the smallest inherent error in the pick. For the digital system, this interval was 20 μs for the blast tests and 10 μs for the microseismic monitoring. The person reading the records will generally be able to judge from relative arrival times which phases are reasonable to pick, and is unlikely to inadvertently mix picks of different phases. There will be some variability in the absolute picks from different persons (pickers), but the internal consistency can be very high. Similar statements apply to the assignment of quality descriptors to a given pick. The picker can readily say whether a low-quality pick is due to a low signal-to-noise ratio, or to an emergent signal, or to some other cause.

Software Timing

Software picks for arrival-time determination are similar to hardware picks in that there are many picking algorithms (*24*). A distinct advantage is the ability to customize, at any desired time, a particular picking algorithm to suit a wide variety of (possibly time-variable) signal conditions. Assignment of quality is also possible, and can overcome some of the difficulty in picking first arrivals using an algorithm that may not be optimized for certain signal types.

Example Comparison

Two methods of obtaining arrival-time picks were compared for ~40 microseismic events which had acceptable location quality. The analog system used a simple voltage threshold exceedance hardware pick which was subsequently screened in software as described earlier. The digital system used interactive manual picks from visual examination of digitized waveforms for the same set of signals used for the hardware picks.

The analog and digital systems were not tied to the same clock. It was necessary, therefore, to arbitrarily adjust the timebase from one set of arrival-time picks to the other. The hardware pick method sets the first hit station (accelerometer with the first exceedance of threshold voltage) to time zero and determines all the other arrival times relative to the first hit accelerometer. The digital waveform system assigns a time to each event from the computer clock.

To obtain a comparison between these two methods, it was assumed that there was no difference between the two pick methods at least one accelerometer (not necessarily the first one hit). The accelerometer with no discrepancy was chosen such that (1) the arrival was impulsive to avoid an obvious late pick associated with an emergent signal, (2) tying to that station did not result in a hardware pick which arrived ahead of the manual pick by more than 10 μs at any other station, and (3) the differences between the two sets of picks were otherwise minimized.

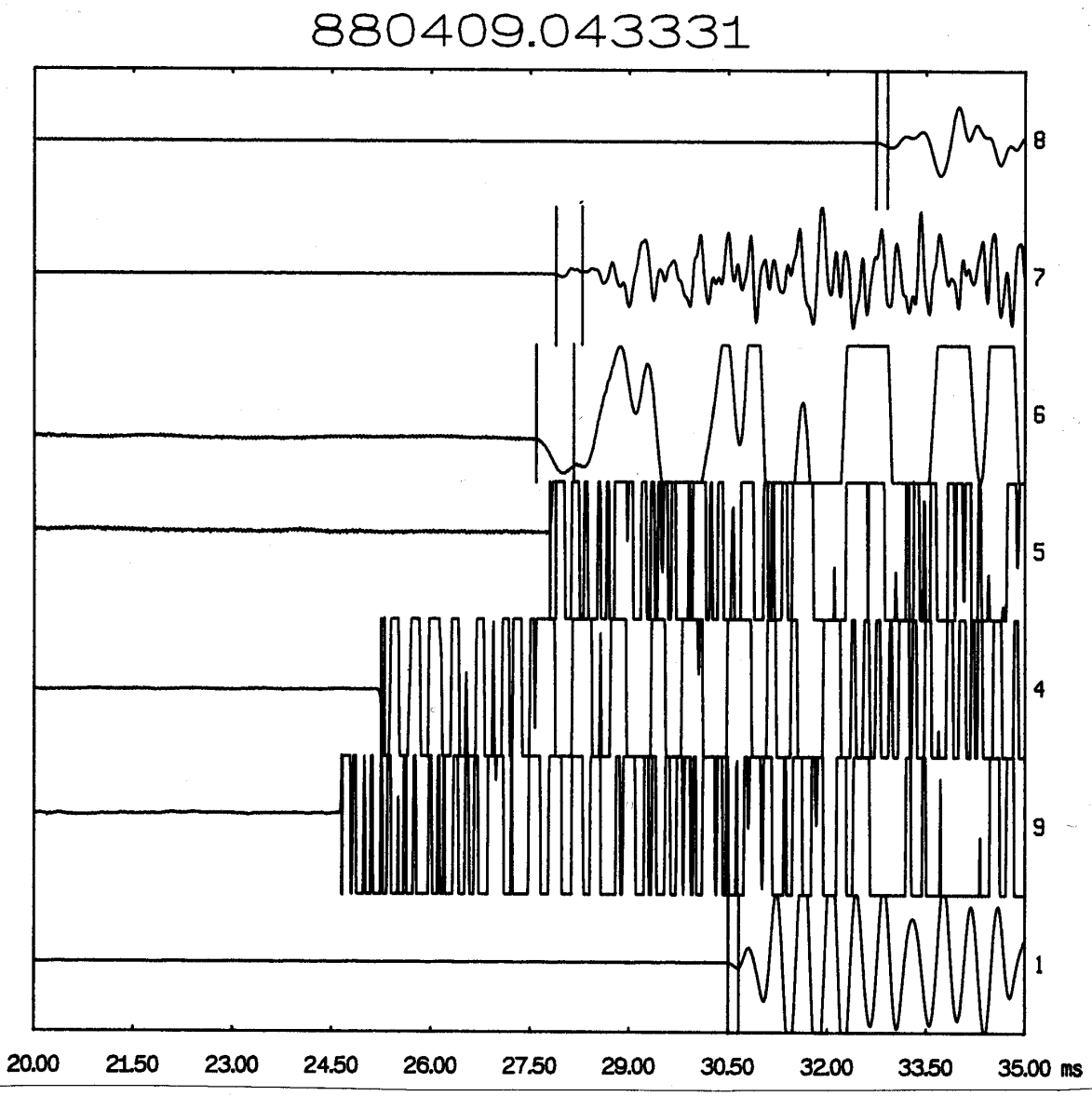

Figure 11.—Example of comparison between manual (first vertical bar on accelerometer waveform) and hardware (second vertical bar on waveform) picks of first arrival times shows typical observed discrepancies.

Figure 11 shows examples of the picks for the two methods. It is clear that the hardware picker is unable to do a good job on the pick at station 6. Station 6 is thought to be bonded to a semi-detached block of rock which provided systematically emergent signals. Station 6 happens to be the first hit station for most of the events of the side-by-side monitoring test: the recorded arrival times at the rest of the stations in the analog system are systematically offset by the error in the first hit station. This leads to significant location errors when the first hit station data is used to form all of the equations for the BLD basis.

Examples of the hardware picking a later phase, a fairly common occurrence, are evident in figure 12. This event was subsequently rejected through the software screening in the analog system.

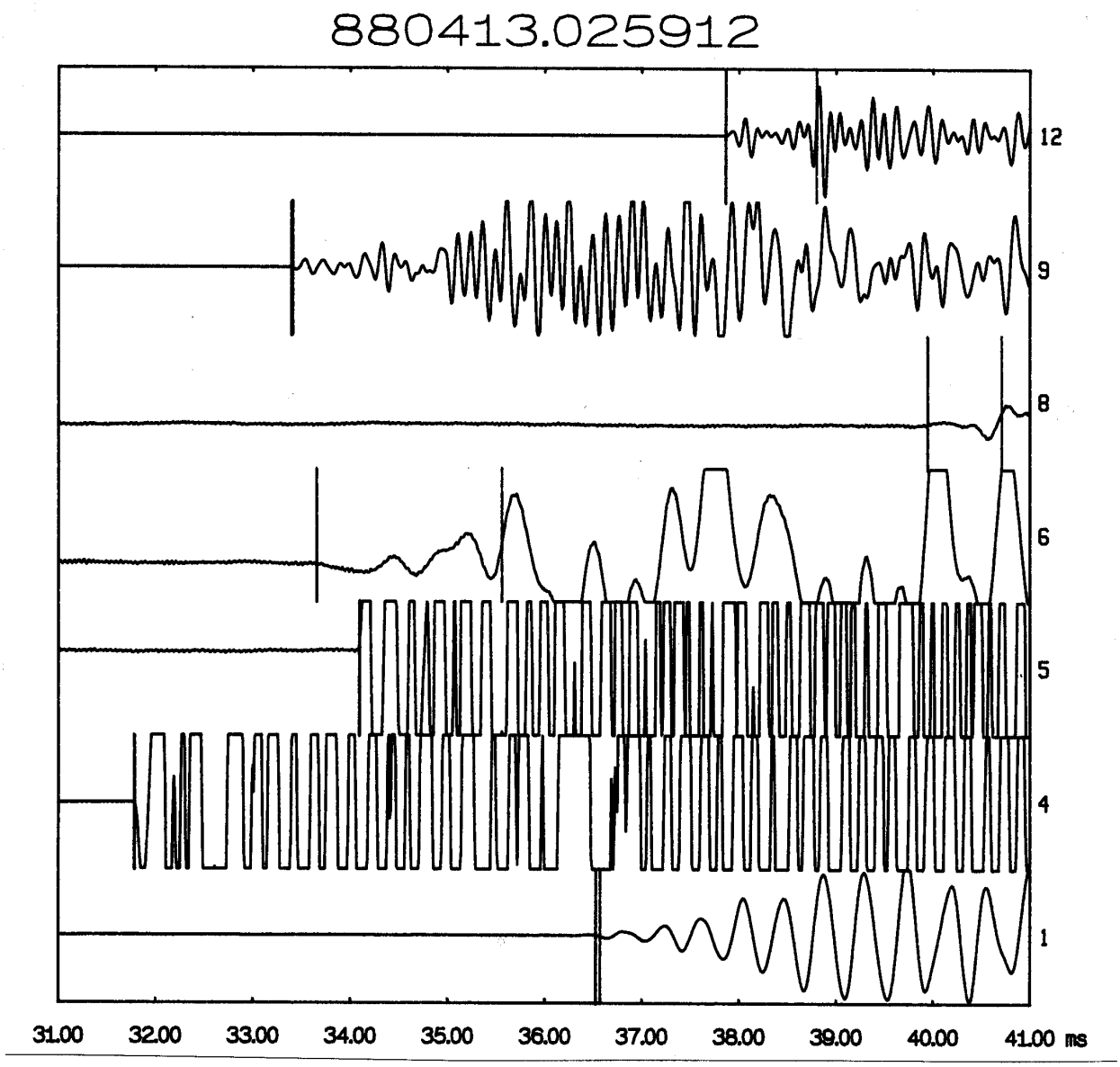

Figure 12.—Example of hardware picks missing first phase (P-wave) and picking later phase.

For the 40 events with acceptable-quality locations, table 4 shows the average difference between the manual and the software-screened hardware picks.[10] (Hardware-pick preprocessing eliminated two picks which differed from the manual picks by as little as 10 μs.) The differences for the 216 arrivals which were analyzed ranged from 0 to 1,170 μs with a distribution that approximated an exponential function with a 142-μs time constant (fig. 13). The average difference is 126 μs, which represents a modest fraction of the average travel time to the first hit accelerometer.

[10]An early prototype version of the first-arrival picking hardware provided four microsecond time resolution and was used in this comparison. Travel-time pick resolution in the standard analog system (100 μs) necessarily yields larger errors.

Table 4.—Difference between hardware and manual picks of first arrival times at nine stations, milliseconds

Event	1	3	4	5	6	7	8	9	12
1	—	0.010	—	T	-0.030	0.030	-0.130	—	—
2	-0.030	-.040	T	-0.010	-.170	—	-.070	-0.020	—
3	.000	-.270	—	T	-.090	—	-.250	-.200	—
4	T	.000	0.010	-.010	-.110	—	-.020	.000	—
5	—	-.120	.010	T	-.120	—	-.110	.000	—
6	—	—	—	T	-.130	-.020	-.150	—	—
7	.020	-.090	—	T	-.060	—	-.500	.010	—
8	T	-.140	—	-.030	-.240	—	-.050	—	—
9	T	-.370	—	.000	-.290	—	-.050	-.020	—
10	-.010	-.110	.020	T	-.290	-.060	-.210	.000	—
11	-.320	-.010	T	-.100	-.420	-.060	-.230	-.030	—
12	—	-.030	.010	T	-.100	-.040	-.060	-.040	—
13	T	—	-.030	-.060	-.240	-.010	-.060	-.050	—
14	T	-.740	-.030	-.030	-.140	-.110	-.490	-.060	—
15	T	—	.000	-.010	-.290	-.070	-.090	-.120	—
16	T	-.350	-.050	-.050	-.270	.000	-.130	-.090	—
17	T	.010	-.040	.000	-.160	-.140	-.070	.000	—
18	T	—	—	-.020	-.130	-.020	-.040	-.070	—
19	T	—	.000	-.030	-.190	.000	-.840	-.390	—
20	—	—	—	-.010	-.210	T	-.030	-.040	—
21	—	—	—	-.010	-.170	-.020	-.050	T	—
22	-.090	—	—	T	-.320	-.050	-.070	.000	—
23	-.170	—	-.060	-.100	-.580	-.410	-.180	T	—
24	.010	—	—	T	-.060	-.030	-.010	-.180	—
25	.000	—	T	.010	-.550	-.050	-.060	-.230	—
26	-.010	—	T	-.010	-.460	-.030	-.060	-.020	—
27	-.130	—	T	.000	-.130	-.050	-.150	-.030	—
28	—	—	-.030	T	-.210	-.020	-.280	-.030	—
29	-.010	—	T	-.020	-.310	-.100	-.060	-.030	—
30	.010	—	T	-.170	-.250	.000	-.260	.000	—
31	T	—	-.040	-.040	-.050	-.020	-.010	-.260	—
32	-.060	—	T	-.040	-.150	-.030	-.040	-.040	—
33	.000	—	-1.170	T	-.290	-.130	-.080	-.010	—
34	-.060	—	T	.000	—	-.030	-.100	-.040	—
35	-.020	—	—	T	-.190	-.500	-.540	-.020	—
36	-.080	—	T	.000	-.030	—	-.050	-.020	-0.290
37	—	—	—	.040	—	—	-1.070	-.050	T
38	-.020	—	—	-.010	-.310	—	-.060	T	-.200
39	.000	—	.010	T	-.130	—	-.570	—	-.240
40	.010	—	-.040	T	-.230	—	-.050	-.360	—
Mean	.050	.164	.097	.031	.213	.075	.183	.075	.243
Std dev ..	.077	.208	.287	.039	.132	.116	.233	.103	.045

— Arrival time not available for one or both systems.
T Time bases tied at this station.

An example of the effect of the difference between the hardware-determined arrival-time picks of the analog system and the arrival-time picks determined by visual inspection of waveforms is seen in figure 14. Here, a subset of the 52 events, which were well-located by both the analog and digital systems, were relocated using the same values of velocity and accelerometer coordinates and using identical numerical location techniques. Arrival-time measurements from both the prescreened analog picks and the manual picks were culled to include only data from accelerometers in common. The differences between the locations shown in pairs in figure 14 are solely due to the difference between hardware arrival-time picks and unweighted manual picks of arrival time. The magnitude of the average three-dimensional discrepancy vector is 3.7 m.

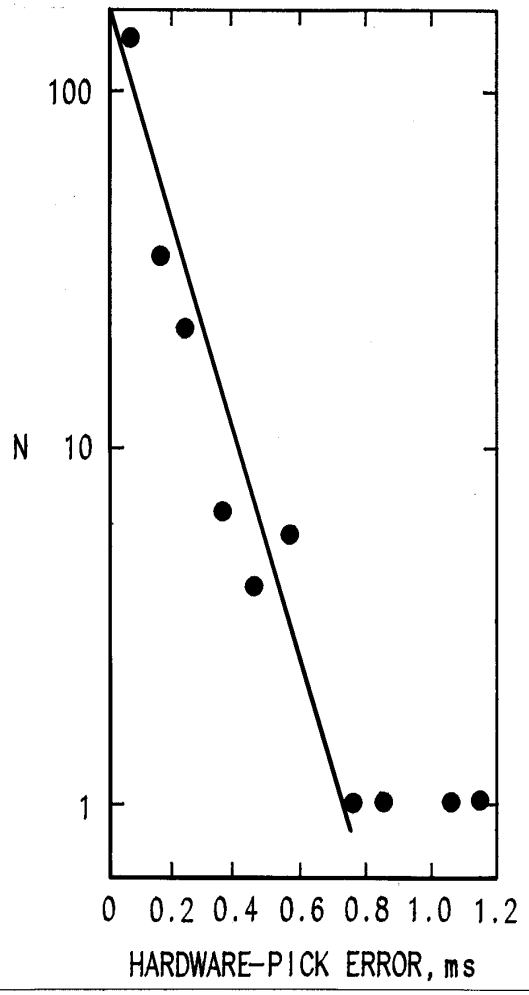

Figure 13.—Histogram showing difference between hardware and manual travel-time picks. Straight line indicates exponential fit to errors less than 0.8 ms.

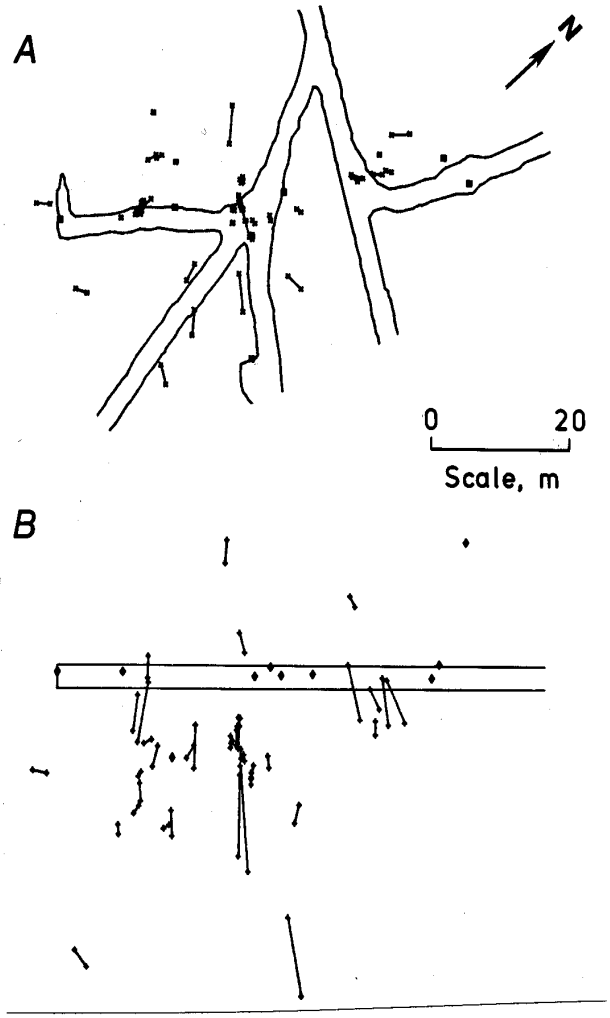

Figure 14.—Comparison between 40 event locations calculated using hardware and manual picks of arrival times with all other parameters identical. Lines connect each set of solutions. *A*, Plan view; *B*, vertical section looking northwest.

To allow comparison of travel-time pick errors with discrepancies resulting from accelerometer position measurement errors, figure 15 shows another defined set of 1,000 events in the control volume. Event locations calculated using exact travel-time data with controlled random errors added are shown with connecting lines. The errors were randomly selected subject to the constraint of the observed exponential distribution of travel-time-pick errors. The average three-dimensional discrepancy vector for the events in this control volume has a magnitude of 2.8 m. Location calculations using error values appropriate to manual first-arrival picking resulted in average three-dimensional discrepancy vector magnitudes of 0.7 m.

SEISMIC WAVE VELOCITY

Influence of Mine Openings

Mine openings represent a distinct source of heterogeneity in the seismic velocity structure. The seismic velocity in air (330 m/s) is so low that most of the seismic energy travels around the periphery of the opening. As a practical means of assessing the influence of openings on microseismic event locations, the measured travel times were investigated (as opposed to the much more involved task of calculating accurate raypaths through heterogeneous

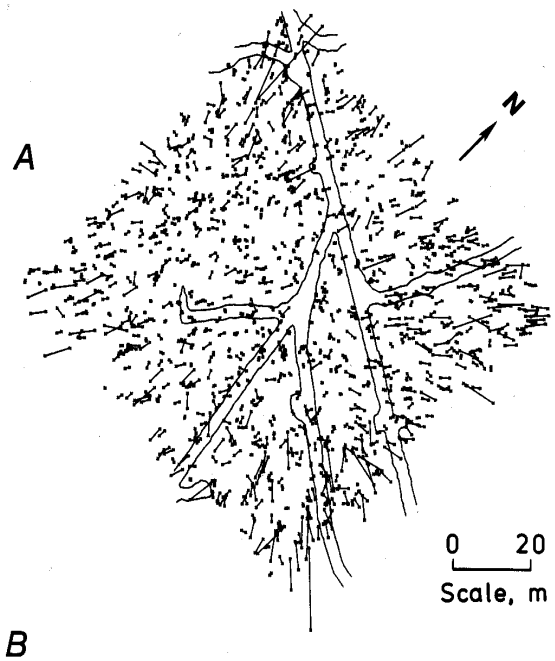

Figure 15.—Comparison between 1,000 defined event locations and locations calculated with hardware-based first-arrival time pick errors added to exact travel times. Lines connect defined locations with calculated locations. *A*, Plan view; *B*, vertical section view looking northwest.

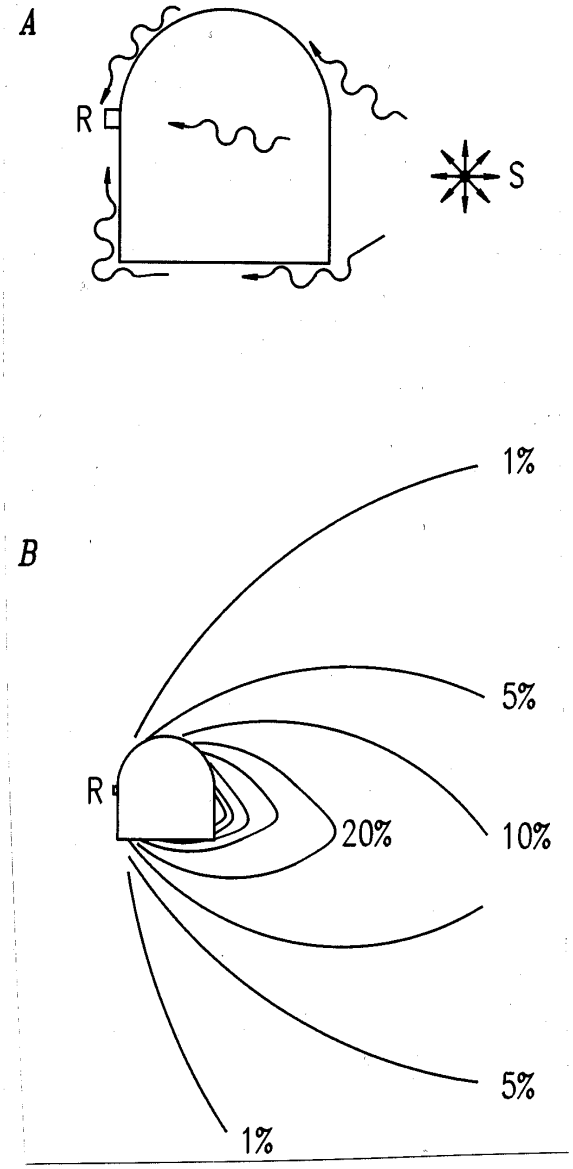

Figure 16.—Influence of mine openings on seismic wave travel times. *A*, Approximate short-wavelength source (S) to receiver (R) raypaths near mine openings; *B*, percentage difference in travel times between virtual straight raypath and path around mine opening as function of seismic source location.

velocity structures with extreme acoustic impedance mismatches) and contrasted with the travel times that would be expected without mine openings. Consider the schematic in figure 16*A* showing a receiver attached to a mine opening and seismic waves emanating from a source within the rock on the opposite side of the opening. For sufficiently long wavelengths (greater than 10 times the mine-opening circumference), the presence of the mine opening does not affect the wave propagation (25). In the present study, however, the observed wavelengths of first arrivals from microseismic events (1 to 5 m) are generally on the order of the smallest mine-opening dimensions (1 to 3 m), and hence their influence on first-arrival times must be estimated.

Since the first signal detected at the receiver travels along a minimum-time travel path (Fermat's principle), the fastest path, in the short wavelength limit, is through the solid rock medium around the mine opening. This travel time was estimated for various seismic source positions and compared with the travel time for a straight raypath without the mine opening. Figure 16*B* illustrates the percentage difference in travel time between these two paths as a function of position. The largest discrepancies (delays) occur for seismic sources positioned immediately adjacent to mine openings. Note the reduced error associated with the more rounded opening. In practice, mine openings often fall between these two extreme geometries.

Since microseismic events associated with mining activity often occur within a very few mine-opening-dimensions of a mine opening, the travel times measured by source-receiver geometries as shown above are systematically biased to longer times than those associated with the straight line propagation path assumed in the event location process. For events occurring on the same level as the mine openings, where most receiver stations are typically located (e.g., fig. 4), there can be a large proportion of the total number of the received signals that experience interaction with mine openings. The same is true for events occurring near the working stope opening. As the propagation path becomes very long in proportion to the smallest mine-opening dimensions, however, the travel-time delay due to interaction with the mine openings diminishes.

Three additional sources of systematic bias exist for raypaths interacting with mine openings, most of which do not diminish rapidly with increasing distance between the source and the opening. First, there is a reduction in amplitude of received signals due to (1) a factor of 5 reduction in amplitude response in the shadow zone region of the mine opening (source placed on right-hand side of figure 16*A*) (*25*) for typical wavelengths associated with observed microseismic events, and (2) the amplitude response of the rib-mounted accelerometers is negligible at angles of incidence close to 90°. Second, there is an increase in the seismic wave rise time of approximately 40% for the shadow zone position compared with an accelerometer mounted on the wave-incident side of the mine opening (*25*). Third, a blasting-related low-velocity damage zone surrounds mine openings. Additional shadowing is produced when raypaths encounter this low-velocity region and suffer a further reduction in wave amplitudes. The reduced amplitudes and slower rise time can provide a systematic late arrival-time pick. The low-velocity zone also yields longer travel times than would be found for paths far removed from mine openings due either to travel through the slower velocity structure or through a faster, but longer path. The net result of all the above influences is to further increase the travel time over the straight-raypath travel time through a constant velocity medium.

On the basis of the two-dimensional calculations presented in figure 16*B*, one might expect that an event location, calculated assuming an isotropic velocity, would be displaced away from the mine opening. The actual picture is much more complicated as illustrated in the following example. Filled triangles in figure 17 show 12 arbitrarily selected event locations near mine openings with vertical coordinates positioned at the mine opening center. Travel times to each receiver were estimated assuming a (short wavelength) raypath which travels around the mine opening along the fastest path; no other travel-time bias associated with mine openings was included. The corresponding calculated event locations are shown as plus symbols. Some events are displaced away from, and some toward, mine openings; most discrepancy vectors (linking actual and calculated positions) have a similar apparent trend. In this particular example, which was chosen to maximize the influence of mine openings, the average three-dimensional discrepancy vector is on the order of 1.2 m. The relative positions of the event location, the mine openings, and the nearest receivers with delayed signals determine the direction of mislocation.

Seismic Velocity Measurements

Seismic wave velocities were calculated using the calibration-blast test data. The apparent velocity was obtained from the ratio of wave propagation path lengths, measured along a straight line between the blast site and each accelerometer, to the measured P-wave travel times.

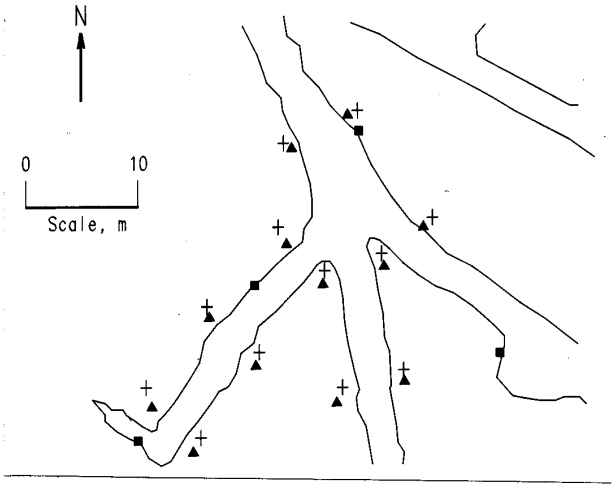

Figure 17.—Influence of mine-opening-related travel-time delays on calculated event locations. Defined event locations (filled triangles); event locations calculated with estimated travel-time delays (+); nearby receivers (filled squares).

Since the first signal detected at the receiver travels along a minimum-time travel path (Fermat's principle), the fastest path, in the short wavelength limit, is through the solid rock medium around the mine opening. This travel time was estimated for various seismic source positions and compared with the travel time for a straight raypath without the mine opening. Figure 16*B* illustrates the percentage difference in travel time between these two paths as a function of position. The largest discrepancies (delays) occur for seismic sources positioned immediately adjacent to mine openings. Note the reduced error associated with the more rounded opening. In practice, mine openings often fall between these two extreme geometries.

Since microseismic events associated with mining activity often occur within a very few mine-opening-dimensions of a mine opening, the travel times measured by source-receiver geometries as shown above are systematically biased to longer times than those associated with the straight line propagation path assumed in the event location process. For events occurring on the same level as the mine openings, where most receiver stations are typically located (e.g., fig. 4), there can be a large proportion of the total number of the received signals that experience interaction with mine openings. The same is true for events occurring near the working stope opening. As the propagation path becomes very long in proportion to the smallest mine-opening dimensions, however, the travel-time delay due to interaction with the mine openings diminishes.

Three additional sources of systematic bias exist for raypaths interacting with mine openings, most of which do not diminish rapidly with increasing distance between the source and the opening. First, there is a reduction in amplitude of received signals due to (1) a factor of 5 reduction in amplitude response in the shadow zone region of the mine opening (source placed on right-hand side of figure 16*A*) (*25*) for typical wavelengths associated with observed microseismic events, and (2) the amplitude response of the rib-mounted accelerometers is negligible at angles of incidence close to 90°. Second, there is an increase in the seismic wave rise time of approximately 40% for the shadow zone position compared with an accelerometer mounted on the wave-incident side of the mine opening (*25*). Third, a blasting-related low-velocity damage zone surrounds mine openings. Additional shadowing is produced when raypaths encounter this low-velocity region and suffer a further reduction in wave amplitudes. The reduced amplitudes and slower rise time can provide a systematic late arrival-time pick. The low-velocity zone also yields longer travel times than would be found for paths far removed from mine openings due either to travel through the slower velocity structure or through a faster, but longer path. The net result of all the above influences is to further increase the travel time over the straight-raypath travel time through a constant velocity medium.

On the basis of the two-dimensional calculations presented in figure 16*B*, one might expect that an event location, calculated assuming an isotropic velocity, would be displaced away from the mine opening. The actual picture is much more complicated as illustrated in the following example. Filled triangles in figure 17 show 12 arbitrarily selected event locations near mine openings with vertical coordinates positioned at the mine opening center. Travel times to each receiver were estimated assuming a (short wavelength) raypath which travels around the mine opening along the fastest path; no other travel-time bias associated with mine openings was included. The corresponding calculated event locations are shown as plus symbols. Some events are displaced away from, and some toward, mine openings; most discrepancy vectors (linking actual and calculated positions) have a similar apparent trend. In this particular example, which was chosen to maximize the influence of mine openings, the average three-dimensional discrepancy vector is on the order of 1.2 m. The relative positions of the event location, the mine openings, and the nearest receivers with delayed signals determine the direction of mislocation.

Seismic Velocity Measurements

Seismic wave velocities were calculated using the calibration-blast test data. The apparent velocity was obtained from the ratio of wave propagation path lengths, measured along a straight line between the blast site and each accelerometer, to the measured P-wave travel times.

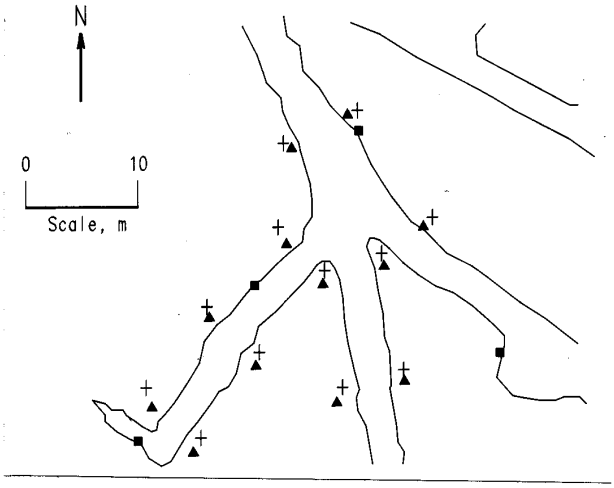

Figure 17.—Influence of mine-opening-related travel-time delays on calculated event locations. Defined event locations (filled triangles); event locations calculated with estimated travel-time delays (+); nearby receivers (filled squares).

Figure 18 shows in plan view the apparent velocities measured along unobstructed raypaths. (For the other stations, some part of a hypothetical straight raypath would have traversed a drift or a mined-out stope.) The values shown are average values from five tests. The repeatability of the travel-time measurements in the calibration blast tests was typically ±1.5%.

The apparent P-wave velocity varies by as much as 50% along the different unobstructed raypaths. The lowest velocity measurement (3,260 m/s or 10,900 ft/s) occurs over the shortest path, which is entirely near the active stope. The highest velocity (4,950 m/s) occurs over one of the longest paths which travels through a greater proportion of undisturbed material far removed from mine openings. Additional velocity measurements made over different paths between the stopes of figure 4 using hammer sources ranged from 4,100 to 5,700 m/s. The lowest values of velocity were observed over paths most affected by mining-induced fracturing near mine openings.

The travel path from source to receiver will not be a straight line, but a curved path when there are such large spatial variations in seismic velocity (>15%, *26*). The location calculations assume simple straight raypaths. Thus the constant seismic velocity model is only an approximation to the actual medium.[11] In accepting the use of a constant velocity model, two questions must be posed: (1) which value of velocity should be used; and (2) how does this simplification of the velocity structure affect the accuracy of the location? This latter question is deferred to the discussion section.

An average velocity was determined by plotting the measured travel time against the straight-line distance between the calibration blast site and each receiver (fig. 19). For raypaths interacting with mine openings, a small path-dependent adjustment has been applied to the straight-ray propagation distance. The slope of a straight-line fit to the data, through the origin, is taken to represent the average velocity. At the 95% confidence level, this average value of velocity is 5,000 ±200 m/s. It must be kept in mind that since the velocity varies as a function of position (fig. 18) there is no single correct value of average velocity. An appropriate average value for a source located at the calibration blast site is 5,000 m/s. Significant location errors will result for *any one* average value of velocity since raypaths will in general traverse mine rock with seismic velocities varying over the observed range (up to 50%).

Location discrepancies for the analog and digital systems due to systematic uncertainties in the average value of velocity are now examined. Figure 20 shows the control volume with 1,000 defined event locations and event locations calculated using the SW-GBM method with a 4% systematic error in velocity (equivalent to the 200 m/s uncertainty determined from the data in figure 19). The average magnitude of the resulting three-dimensional discrepancy vectors is 1.2 m. This figure represents the lower

[11]The relative amounts of spatial variation in velocity due to geologic structure variations and mining-induced fracturing are now being investigated in two-dimensional seismic tomography experiments at this site.

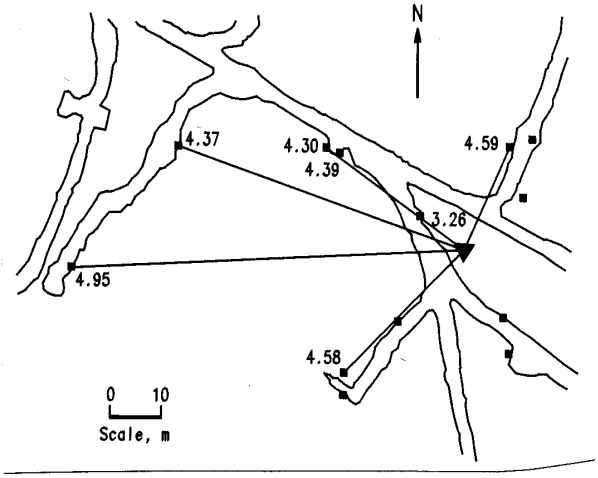

Figure 18.—Apparent seismic velocities (kilometer per second) calculated for straight raypaths in calibration blast tests. Filled triangle indicates calibration blast location. Filled squares are receiver locations.

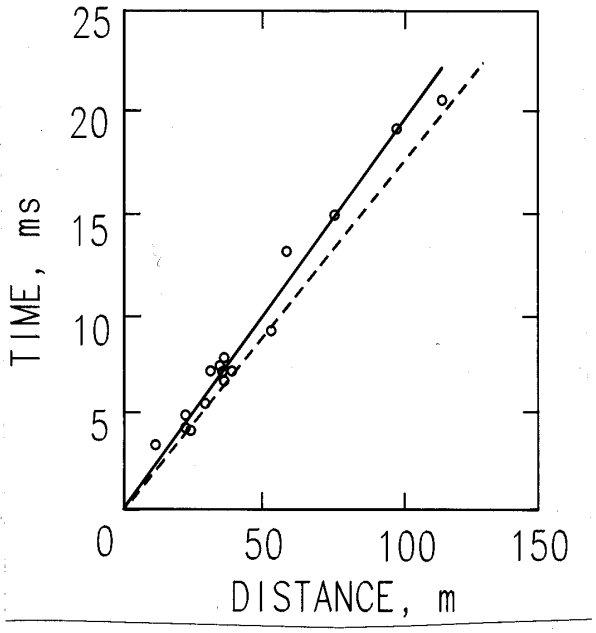

Figure 19.—Measured travel times and straight-line distances between all source and receiver sites for calibration blast tests. Dashed line represents 5,640 m/s (13% higher than 5,000 m/s), a velocity that may be more appropriate for unfractured rock far removed from mine openings.

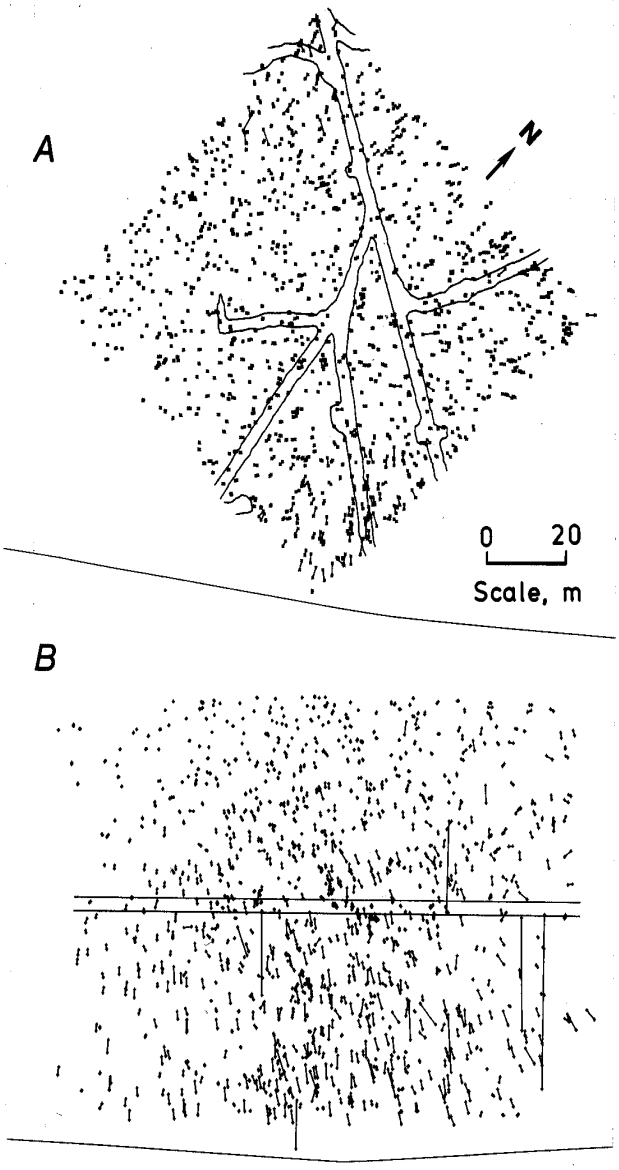

Figure 20.—Influence of 4% systematic velocity error (5,200 vs. 5,000 m/s) on calculated location of 1,000 defined events in control volume. *A*, Plan view; *B*, vertical section looking northwest.

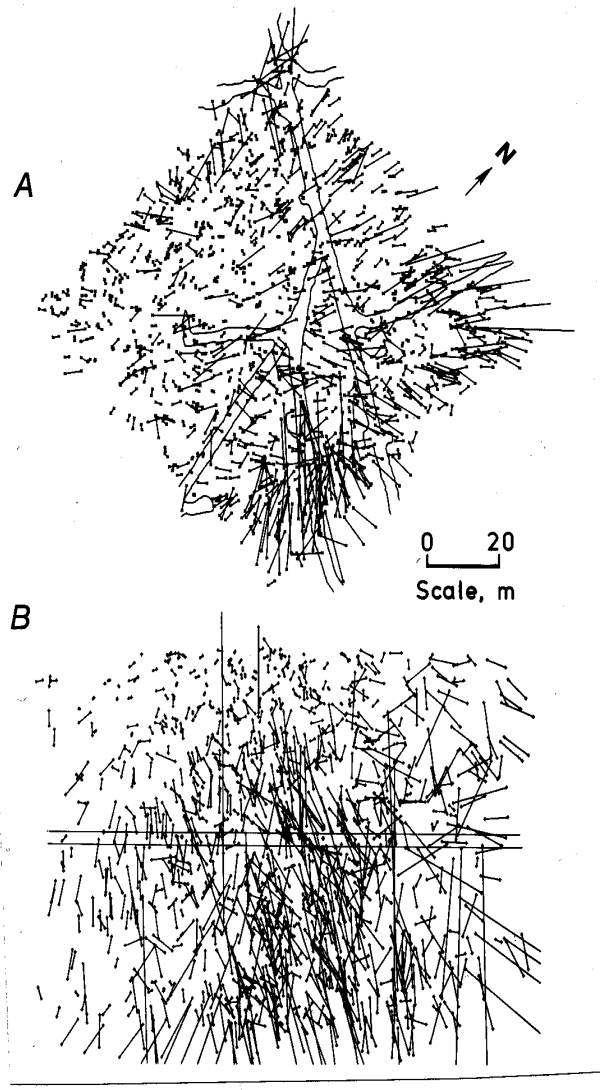

Figure 21.—Influence of 13% systematic velocity error (5,640 vs. 5,000 m/s) on calculated location of 1,000 defined events in control volume. *A*, Plan view; *B*, vertical section looking northwest.

limit of location uncertainty associated with a systematic velocity error in a truly constant velocity medium.

A velocity of 5,640 m/s was previously determined for use with the analog system in similar calibration blast surveys in a different part of the Galena Mine. Observed apparent velocities ranged from 4,200 to 6,700 m/s. The median value of 5,640 m/s (dashed line in figure 19), which is a representative value for high-velocity undisturbed paths, has subsequently been used as the velocity for the mine-wide-network monitoring experiment. Figure 21 illustrates the location discrepancies which result when 5,640 m/s is used in an area where 5,000 m/s may be a better average velocity (i.e., a 13% systematic discrepancy in the velocity). The average magnitude of the location discrepancy vectors is 7.0 m. This value is reduced to 2.1 m when a 4% error is assumed for an average velocity of 5,000 m/s and events are located using the BLD method in the analog system.

DISCUSSION

The relative contributions of measurement errors in accelerometer positions, travel-time picks, and average velocity to errors in microseismic event locations can be assessed for the analog system by comparing figures 10, 15, and 21. Table 5 summarizes the average magnitudes of the discrepancy vectors of the 1,000 random events in the control volume for each source of error. A composite figure incorporating these three sources of error is shown in figure 22. A similar figure for the digital system is shown in figure 23 and summarized in table 5. The overall spatial discrepancies for the digital system are approximately five times smaller than for the analog system. When the lower average velocity value of 5.0 km/s is assumed with a 4% error for the analog system, the average composite discrepancy vector magnitude is reduced to a little less than three times the value for the digital system.

Table 5.—Average calculated location-discrepancy vector magnitudes, meters

	Analog	Digital
Accelerometer position	2.3	0.1
Travel time	2.8	.7
Velocity	7.0	1.2
Composite	7.7	1.4

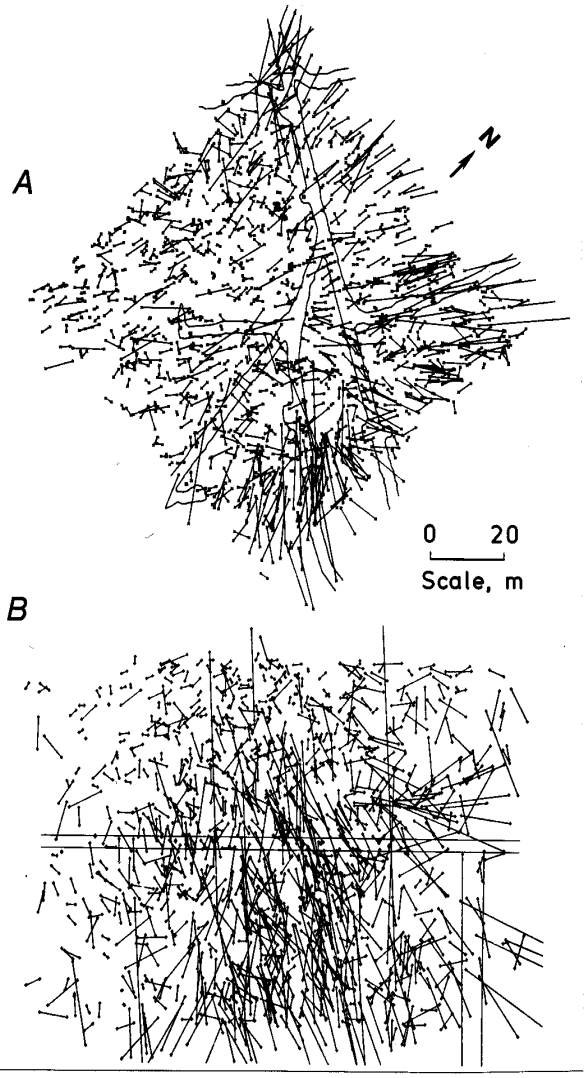

Figure 22.—Composite plot for analog system showing location discrepancies calculated using measured errors in accelerometer position, arrival-time picks, and assumed isotropic velocity. *A*, Plan view; *B*, vertical section looking northwest.

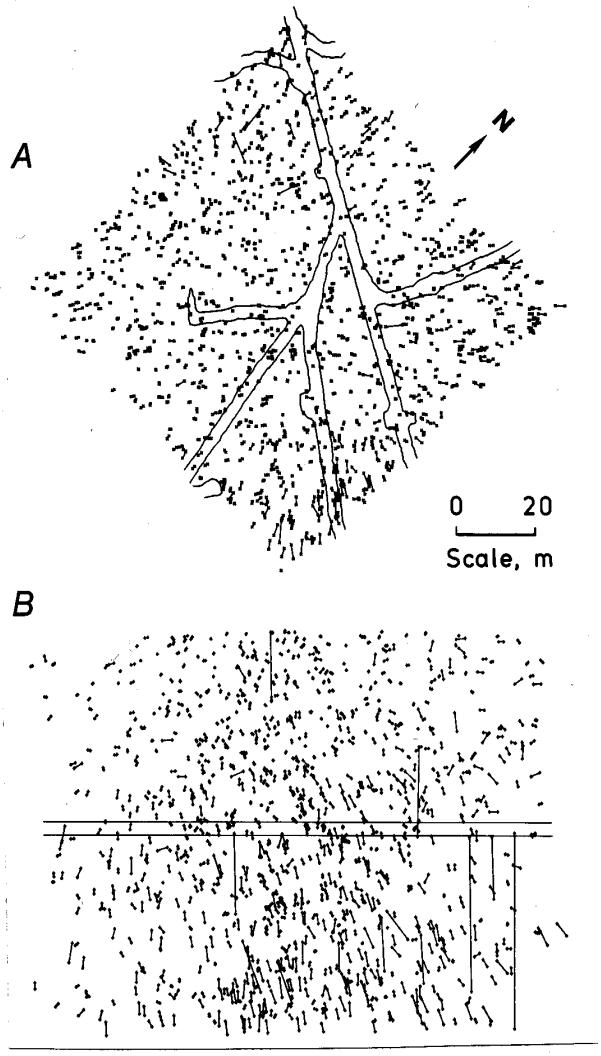

Figure 23.—Composite plot for digital system showing location discrepancies calculated using measured errors in accelerometer position, arrival-time picks, and assumed isotropic velocity. *A*, Plan view; *B*, vertical section looking northwest.

If the significant sources of uncertainty in microseismic event locations have been correctly identified and characterized, then the discrepancy vectors in figure 23 should be consistent with the observed discrepancies between surveyed and calculated calibration blast locations. Figure 24 shows the calibration blast locations for the digital system and axes of the SVD spatial uncertainty ellipsoids of 95% confidence. A comparison between figures 23 and 24 reveals that the calculated and observed discrepancy vectors are not equal. Near the calibration blasts, the composite discrepancy vectors estimated for the digital system (<1 m; fig. 23) are much smaller than the observed discrepancies (~10 m; fig. 24). This discrepancy is presumably attributable to the fact that the heterogeneous seismic velocity structure at the experiment site does not adequately conform to the assumed constant velocity model.

Other observations from figure 24 are noted as follows: (1) The computed 95% confidence error ellipsoids do not encompass the surveyed position of the blast site. As previously noted, the ~10 m offset of the surveyed position from the calculated locations indicates a location accuracy of approximately ±10 m. (2) The precision of the locations (±1 m) is limited by the precision of the travel-time picks and is illustrated by the ±1 m clustering of four of the calculated blast positions. These four locations were determined using arrivals from the same set of 17 receivers with only slight variations in travel-time picks. (3) A smaller subset of 10 arrivals was available for the location of the fifth blast, which is offset from the other four. As the relative arrival times were the same as for the other four locations, this offset indicates the significant influence of receiver array geometry. (4) The error ellipsoids of all of the blast locations have the same approximate magnitude, aspect ratio, and spatial orientation.

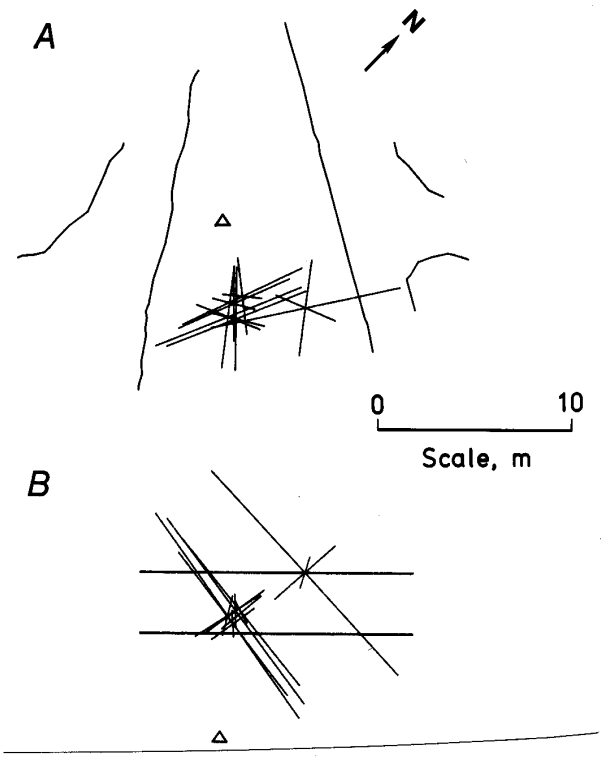

Figure 24.—Calibration blast locations (skewed triad symbols) from digital system illustrating magnitude, shape, and orientation of 95% confidence SVD error ellipsoids. Surveyed blast position is represented by filled triangle. *A*, Plan view; *B*, vertical section looking northwest.

The fact that none of the spatial uncertainty error ellipsoids encompass the surveyed blast position is consistent with the contention that the isotropic velocity model does not adequately conform to the actual velocity structure. Recall that the SVD error ellipsoid provides confidence limits on the location uncertainty if the errors are normally distributed. Since the deviation of a heterogeneous velocity structure from a uniform velocity model does not in general result in normally distributed velocity errors (or resultant measured travel times), the calculated SVD error ellipsoids do not, as observed in figure 24, adequately describe the constraint on the source locations in this situation. Use of a more realistic (heterogeneous) velocity structure is required so that the error ellipsoids more closely reflect the constraint on the solution due to the actual measurement errors.

A location discrepancy of 10 m is not expected for all controlled-source tests. The various factors providing constraint on the source locations (e.g., array geometry, number of reporting receivers, degree of local deviation of velocity structure from assumed model, etc.) vary over all combinations so that a single number cannot effectively characterize source location accuracy for all sources. Constraint on the source location solution will be better than 10 m in some situations and much worse in others.

In summary, the failure of the isotropic velocity model to adequately describe wave propagation at this site appears to represent the largest systematic source of uncertainty in event locations for both the analog and digital systems. To significantly increase the accuracy of event locations in any part of the mine covered by the array, a more accurate representation of the velocity structure is required.

While considerable effort toward an improved velocity model for research purposes is warranted, continued use of constant isotropic velocity models in routine microseismic monitoring is appropriate. The value of this health, safety, and productivity tool is negligibly affected by the observed location uncertainty, at least when an appropriate average velocity is used. An event location accuracy of ±10 m in a mine where working areas are separated by hundreds of meters and are individually monitored, readily

allows the identification of the specific working area that is associated with microseismic activity (and those that are not). In individual stopes of dimensions 60 by 100 m, it can still be determined approximately where in the stope this activity is taking place. Furthermore, the determination of rates of microseismic activity for daily mine stability assessments, are not at all affected.

The improvements in event location accuracy which are attainable by reducing random measurement errors, e.g., surveying the accelerometer coordinates and manually picking first-arrival times, are small in comparison to the improvements which are possible if the spatial variation in seismic velocity is characterized and used in the event location process. The increased effort required by the precision measurement procedures is not warranted for routine mine monitoring purposes until more accurate seismic velocity models are developed. For the development of rock burst prediction and control strategies based on an understanding of the mechanics of rock burst processes, increases in event location accuracy are essential. For example, since large stress gradients are sustained over distances of less than 20 m, especially near mine openings, discontinuity structures cannot be located confidently in even the appropriate stress regime with a location accuracy of ±10 m. Thus, mine stability analyses based on the proposed uses of microseismicity (e.g., discontinuity delineation, determination of slip directions, etc.) require an increase in event location accuracy.

There are several possible approaches for reducing event location uncertainty via characterization of the inhomogeneous velocity structure. Seismic wave travel times can be measured in individual monitoring areas using active seismic sources (*27-29*), and/or relative arrival times can be measured from passive seismic sources (*30*) and used in curved raypath tomographic reconstructions of the three-dimensional velocity structure. Alternatively, a simplified model structure using constant values of velocity (fig. 25) representing intact rock, air in mine openings, sand in backfilled areas and a fractured halo region surrounding mine openings, may provide acceptable improvements in event location accuracy.

There are advantages and disadvantages to each approach. Active seismic tomography allows the controlled placement of seismic sources at known positions and known times. For three-dimensional velocity structure, however, source-receiver placement must also be three-dimensional, which is difficult and expensive since long holes through hard rock generally must be drilled. High resolution in areas of strong velocity gradient is also difficult to achieve unless many measurements are obtained at closely spaced source and receiver positions.

The use of passive sources for tomographic velocity reconstruction, such as microseismicity sources, has the advantage that these seismic sources are generally plentiful and usually accompany the mining process. Also, mines which are presently monitoring microseismicity do not have to acquire additional hardware for data acquisition. A distinct disadvantage in this particular application is that many events are required to be located in the specific volume of rock to be characterized. Thus the large velocity gradients near sensors mounted to ribs in previously excavated mine openings will not be imaged effectively using these sources since most high-angle raypath intersections, which largely determine resolution, are roughly limited to the seismic source region (i.e., stope). Furthermore, one does not have (ready) control over when these sources are activated. Simultaneous determination of event hypocenter and three-dimensional velocity structure is also a much more difficult computing task. This method

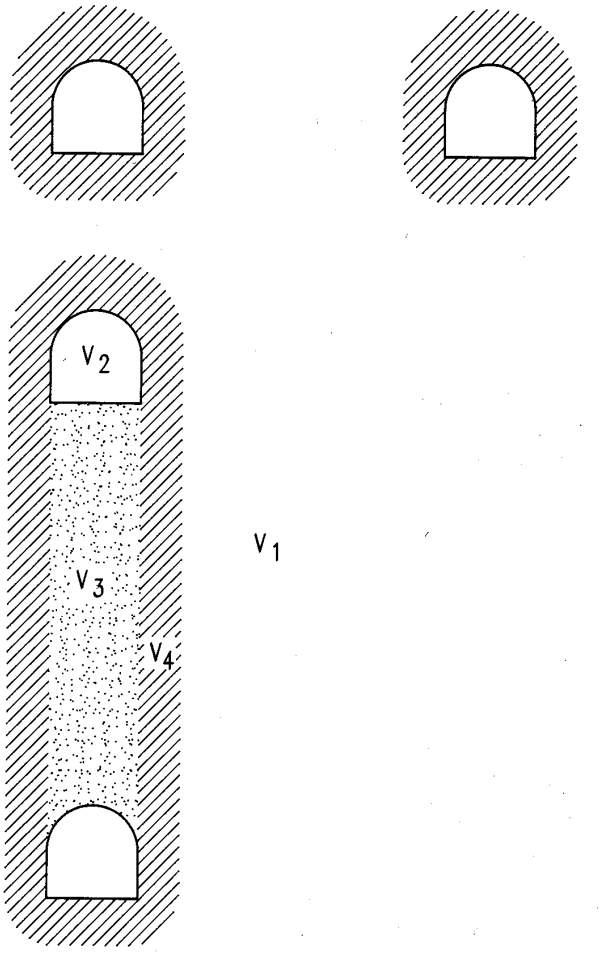

Figure 25.—Vertical cross section through four-component velocity model: V_1 intact rock, V_2 air, V_3 sand, V_4 fractured rock. Geometry is typical of mine openings near stoping areas.

has, however, recently been used to image kilometer-scale velocity heterogeneities in Czechoslovakian coal fields (*30*).

In a hybrid approach, active and passive sources may be combined to compensate for some of the disadvantages of each method. Passive microseismicity sources can provide ray coverage near active working areas (e.g., stope), where it is extremely difficult to maintain electric cable-transducer systems, and active sources can provide coverage wherever and whenever needed.

A three- or four-component velocity model (fig. 25) has relative simplicity as a virtue; however, the effectiveness of this approach must first be assessed by characterizing the three-dimensional velocity structure in detail using some other method. This approach may be attractive for routine monitoring of microseismicity, particularly if it can be demonstrated that there is little variation in velocity within a given model element relative to the velocity differences between elements.

An additional consideration in all of these approaches is the need to continually update the velocity model as mining progresses.

CONCLUSIONS

Various sources of error associated with the microseismic event location process have been examined. Errors in measurements of accelerometer position, travel-time pick and average velocity, including the neglect of the effect of mine openings, were estimated. These errors were used with various numerical location techniques to investigate the accuracy and precision of calculated event locations. One numerical location technique has been found that minimizes spatial location discrepancies for synthetic events embedded in a spatially uniform velocity medium with representative random and systematic errors. This technique uses a direct solution basis function similar to that of Godson (*12*). In general, iterative techniques were found to minimize event mislocation when random measurement errors are present in accelerometer-position and arrival-time data. Event location errors produced by systematic errors in the value of isotropic velocity were found to be minimized when using direct solution methods. The best location solutions, in the presence of a systematic velocity error, are not necessarily those producing a minimum travel-time residual, as is most often assumed.

Through the analysis of a series of calibration test blasts, it has been shown that (1) the location *precision* of blasts and microseismic events at the test site can be ± 1 m and is currently limited by the precision of the first arrival time picks; (2) the location *accuracy*, for both the analog and digital systems, can be ± 10 m and is currently limited by inadequate modeling of the velocity structure; and (3) spatial variations in the apparent velocity exceed 50% due largely to velocity reductions associated with fractured rock surrounding mine openings. To improve location accuracy, the constant isotropic velocity model and straight raypaths must be abandoned for a spatially variable velocity structure with curved raypaths.

While the event location precision for the digital system is approximately a factor of 5 better than for the analog system, the difference in accuracy is much less pronounced.

The observed accuracy is sufficient for routine microseismic monitoring in the mine environment, but is insufficient for detailed analyses of the deformation mechanics in these media.

With the increase in event location accuracy that is possible with a more realistic (heterogeneous) velocity model, significant improvements can be made in delineating the position, orientation, and areal extent of discontinuities actively participating in mining-induced deformation using microseismic event locations.

REFERENCES

1. Swanson, P. L., and F. M. Boler. Application of AE/MS Waveform Analysis to Hazard Detection, Evaluation, and Control in Underground Mining. Paper in Progress in Acoustic Emission IV (Proc. 9th Intl. Acoustic Emission Symp., Kobe, Japan, Nov. 14-17, 1988). The Japanese Society for Non-Destructive Inspection, 1988, pp. 303-310.

2. Fairhurst, C. (ed.). Rock Bursts and Seismicity in Mines (Proc. 2nd Intl. Symp. Rockbursts and Seismicity in Mines, Minneapolis, MN, June 8-10, 1988). Balkema, 1990, 439 pp.

3. Billington, S., F. M. Boler, P. L. Swanson, and L. H. Estey. P-Wave Polarity Patterns from Mining-Induced Microseismicity in a Hard-Rock Mine. Paper in Proceedings of the 31st U.S. Symposium on Rock Mechanics, ed. by W. A. Hustrulid and G. A. Johnson (Golden, CO, June 18-20, 1990). Balkema, 1990, pp. 931-938.

4. Goodman, R. E., and G. Shi. Block Theory and Its Application to Rock Engineering. Prentice-Hall, 1985, 338 pp.

5. Coughlin, J. P., and C. D. Sines. Field Trials of a Portable Microseismic Processor Recorder. BuMines IC 9022, 1985, 8 pp.

6. Steblay, B. J., T. Swendseid, and B. Brady. Innovative Microseismic Rock Burst Monitoring System. Paper in Rock Bursts and Seismicity in Mines (Proc. 2nd Intl. Symp. Rockbursts and Seismicity in Mines, Minneapolis, MN, June 8-10, 1988). Balkema, 1990, pp. 259-262.

7. Steblay, B. J., B. T. Brady, and E. E. Hollop. A Networked Minewide Microseismic Rock Burst Monitoring System. Paper in Mining for the Future-Trends and Expectations (Pres. at 14th World Min. Congr., Beijing, China, May 14-18, 1990). Pergamon, 1990, pp. 861-867.

8. Boler, F. M., and P. L. Swanson. Computer-Automated Measurement- and Control-Based Workstation for Microseismic and Acoustic Emission Research. BuMines IC 9262, 1990, 9 pp.

9. Blake, W., F. Leighton, and W. I. Duvall. Microseismic Techniques for Monitoring the Behavior of Rock Structures. BuMines B 665, 1974, 65 pp.

10. Ge, M., and H. R. Hardy, Jr. A Statistical Method of Evaluation of AE/MS Source Location Accuracy and Transducer Array Geometry. Paper in Proceedings of 30th U.S. Symposium on Rock Mechanics (WV Univ., Morgantown, WV, June 19-22, 1989). Balkema, 1989, pp. 663-670.

11. Salamon, M. D. G., and G. A. Wiebols. Digital Location of Seismic Events by an Underground Network of Seismometers Using the Arrival Times of Compressional Waves. Rock Mech., v. 6, 1974, pp. 141-166.

12. Godson, R. A., M. C. Bridges, and B. M. McKavanagh. A 32-Channel Rock Noise Location System. Paper in Second Conference on Acoustic Emission/Microseismic Activity in Geologic Structures and Materials, ed. by H. R. Hardy, Jr., and F. W. Leighton (Proc. Conf. PA State Univ., University Park, PA, Nov. 13-15, 1978). Clausthal-Zellerfeld, FRP, Trans. Tech. Publ. D-3392, 1980, pp. 117-161.

13. Press, W. H., B. P. Flannery, S. A. Teukolsky, and W. T. Vetterling. Numerical Recipes: The Art of Scientific Computing. Cambridge Univ. Press, 1986, 818 pp.

14. Klein, R. W. Hypocenter Location Program HYPOINVERSE Part I: Users Guide to Versions 1, 2, 3, and 4. U.S. Geol. Surv. OFR 78-694, 1978, 113 pp.

15. Lee, W. H. K., and J. C. Lahr. HYPO71: A Computer Program for Determining Hypocenter, Magnitude, and First Motion Pattern of Local Earthquakes. U.S. Geol. Surv. OFR 75-311, 1972, 113 pp.

16. Lienert, B. R., E. Berg, and L. N. Frazer. HYPOCENTER: An Earthquake Location Method Using Centered, Scaled and Adaptively Damped Least Squares. Bull. Seism. Soc. Am., v. 76, 1986, pp. 771-783.

17. Dahlquist, G., and A. Bjorck. Numerical Methods. Prentice-Hall, 1974, 573 pp.

18. Niewiadomski, J. Application of Singular Value Decomposition Method for Location of Seismic Events in Mines. Pure and Appl. Geophys., v. 129, 1989, pp. 551-570.

19. Riefenberg, J. A Simplex Method-Based Algorithm for Source Location of Microseismic Events Associated With Underground Mining. Paper in Proceedings of 30th U.S. Symposium on Rock Mechanics (WV Univ., Morgantown, WV, June 19-22, 1989). Balkema, 1989, pp. 655-662.

20. Prugger, A. F., and D. J. Gendzwill. Micro-Earthquake Location: A Non-Linear Approach That Makes Use of a Simplex Stepping Procedure. Bull. Seism. Soc. Am., v. 78, 1988, pp. 799-815.

21. Swanson, P. L. Stress Corrosion Cracking in Westerly Granite: An Examination by the Double Torsion Technique. M.S. Thesis, Univ. CO, Boulder, CO, 1980, 142 pp.

22. Corson, D. R., and W. R. Wayment. Load-Displacement Measurement in a Backfilled Stope of a Deep Vein Mine. BuMines RI 7038, 1967, 51 pp.

23. Science Applications International Corporation. Operations Manual: Microseismic Processor Recorder Model DP-138, 1988, p. 6.

24. Lee, W. H. K., and S. W. Stewart. Principles and Applications of Microearthquake Networks. Academic, 1981, 293 pp.

25. Blair, D. P. Dynamic Modelling of In-Hole Mounts for Seismic Detectors. Geophys. J. R. Astron. Soc., v. 69, 1982, pp. 803-818.

26. Dines, K. A., and R. J. Lytle. Computerized Geophysical Tomography. Proc. IEEE, v. 67, 1979, pp. 1065-1073.

27. Mason, I. M. Algebraic Reconstruction of a Two-Dimensional Velocity Inhomogeneity in the High Hazles Seam of Thoresby Colliery. Geophys., v. 46, 1981, pp. 298-308.

28. Kormendi, A., T. Bodoky, L. Hermann, L. Dianski, and T. Kalman. Seismic Measurements for Safety in Mines. Geophys. Prospect., v. 34, 1986, pp. 1022-1037.

29. Young, R. P., D. A. Hutchins, M. Bostock, and P. Mottahed. Geotomographic Imaging of Collapse/Solution Structures in Potash Mines Using Seismic Methods. Paper in Proceedings of 28th U.S. Symposium on Rock Mechanics (Univ. AZ, Tucson, AZ, June 29-July 1, 1987). Balkema, 1987, pp. 19-27.

30. Jech, J. Seismic Tomography in the Ostrava-Karvina Mining Region. Pure and Appl. Geophys., v. 129, 1989, pp. 597-608.

APPENDIX A.—BASIS FUNCTIONS FOR SOURCE LOCATION

Here the generalized basis functions for determining the source location are given along with an outline of their derivation. In general, it is necessary to obtain both the location (x_0, y_0, and z_0) and the origin time (t_0) of the source assuming a homogeneous and isotropic (spatially constant) medium which transmits (either *P* or *S*) seismic signals at a velocity v. Receiver stations having arrivals of the signal are indexed 1,...,m.

SW-GBM BASIS

To derive the SW-GBM basis function, the travel-time equation 1[1] is squared:

$$v^2t_j^2 - x_j^2 - y_j^2 - z_j^2 = x_0^2 + y_0^2 + z_0^2 - v^2t_0^2 - 2x_jx_0 - 2y_jy_0 - 2z_jz_0 + 2v^2t_j\,t_0.$$

Note that here, unlike the outlines given by Salamon and Wiebols (*11*)[2] or Godson (*12*), the arrivals at receivers are not necessarily ordered in any particular way and the unknown time is cast explicitly in terms of the source origin time, t_0, rather than the travel time to receiver j = 1, t_1. Nonlinear terms in the above equation are removed by subtracting equations of *any* two different receivers, say the jth and kth. A system of linear equations can be obtained using the resulting basis function.

$$x_j^2 - x_k^2 + y_j^2 - y_k^2 + z_j^2 - z_k^2 - v^2(t_j^2 - t_k^2) = 2x_0(x_j - x_k) + 2y_0(y_j - y_k) + 2z_0(z_j - z_k) - 2t_0v^2(t_j - t_k). \quad \text{(A-1)}$$

BLD BASIS

The BLD basis function is obtained similarly in that nonlinear equations of form equation 1 are found for two different receivers, say, j and k, which are then squared and differenced. Then, the origin time of the source (t_0) is replaced with the spatial coordinates of another receiver l. Generalizing the development of Blake (*9*), the starting equation for receiver j is, as stated, essentially equation 1:

$$v(t_j - t_l + t_l - t_0) = [(x_j - x_0)^2 + (y_j - y_0)^2 + (z_j - z_0)^2]^{1/2}, \quad \text{(A-2)}$$

where $t_l - t_\ell$ (i.e., zero) has been added to the travel-time difference from the source to receiver j, and of course t_ℓ is the arrival time of the signal at receiver l. The substitutions

$$d_{l0} = v(t_l - t_0) = [(x_l - x_0)^2 + (y_l - y_0)^2 + (z_l - z_0)^2]^{1/2},$$

$$d_{j0} = [(x_j - x_0)^2 + (y_j - y_0)^2 + (z_j - z_0)^2]^{1/2},$$

$$d_{jl} = v(t_j - t_l), \quad \text{(A-3)}$$

are then used where $d_{l0} \geq 0$ is the distance from receiver l to the source, $d_{j0} \geq 0$ is the distance from receiver j to the source, and $|d_{jl}|$ is the distance the signal has traveled between the time of arrival at receiver j and the time of arrival at receiver l (note that d_{jl} can be either positive or negative or zero). After substituting A-2 into A-3 and squaring,

$$d_{jl}^2 + d_{l0}^2 + 2d_{jl}d_{l0} = d_{j0}^2. \quad \text{(A-4)}$$

The same steps are taken for receiver k and receiver l, yielding

$$d_{kl}^2 + d_{l0}^2 + 2d_{kl}d_{l0} = d_{k0}^2. \quad \text{(A-5)}$$

Equation A-4 is then multiplied by d_{kl} and equation A-5 is multiplied by d_{jl}. The difference of (A-4) * d_{kl} and (A-5) * d_{jl} is taken which, after some simplification, gives a basis function for a different system of linear equations with the unknowns x_0, y_0, z_0:

$$(d_{jl}^2 - x_j^2 - y_j^2 - z_j^2 + x_l^2 + y_\ell^2 + z_\ell^2)d_{kl} - (d_{kl}^2 - x_k^2 - y_k^2 - z_k^2 + x_l^2 + y_l^2 + z_l^2)d_{jl} = 2[d_{kl}(x_l - x_j) - d_{jl}(x_l - x_k)]x_0 + 2[d_{kl}(y_l - y_j) - d_{jl}(y_l - y_k)]y_0 + 2[d_{kl}(z_l - z_j) - d_{jl}(z_l - z_k)]z_0, \quad \text{(A-6)}$$

which is a generalized version of Blake's equation C-11. After the spatial coordinates x_0, y_0, and z_0 have been found, an estimate of the origin time t_{0i} can easily be obtained as follows. Estimates of t_{0i} are calculated for each receiver i = 1,...,m

$$t_{0i} = \frac{1}{v}[(x_i - x_0)^2 + (y_i - y_0)^2 + (z_i - z_0)^2]^{1/2}, \quad \text{(A-7)}$$

which are then averaged to obtain a value for t_0.

[1]Equation numbers without an A- prefix refer to equations in the main text.

[2]Italic numbers in parentheses refer to items in the list of references preceding the appendix.

FULL-GRADIENT BASIS

The basic premise for the gradient basis is that it has a function of n unknowns (here n = 4, i.e. x_0, y_0, z_0, and t_0) with m constraints (here m = number of receivers with arrival time information). If $m \geq n$, a solution is attempted. The starting equation is again equation 1 which will be called a function f() of the unknowns:

$$f(t_0, x_0, y_0, z_0) = [(x_i - x_0)^2 + (y_i - y_0)^2 + (z_i - z_0)^2]^{1/2} - v(t_i - t_0) = 0.$$

A Taylor series expansion can be used to obtain a linear approximation to f() in terms of an approximate solution (t_0', x_0', y_0', z_0')

$$0 = f(t_0, x_0, y_0, z_0) \simeq f(t_0', x_0', y_0', z_0') + (t_0 - t_0') \frac{\partial f}{\partial t_0}(t_0') + (x_0 - x_0') \frac{\partial f}{\partial x_0}(x_0') + (y_0 - y_0') \frac{\partial f}{\partial y_0}(y_0') + (z_0 - z_0') \frac{\partial f}{\partial z_0'}(z_0')$$

where the partial derivatives are simply

$$\frac{\partial f}{\partial t_0} = v$$

$$\frac{\partial f}{\partial x_0} = (x_0 - x_i)[(x_i - x_0)^2 + (y_i - y_0)^2 + (z_i - z_0)^2]^{-1/2}$$

$$\frac{\partial f}{\partial y_0} = (y_0 - y_i)[(x_i - x_0)^2 + (y_i - y_0)^2 + (z_i - z_0)^2]^{-1/2}$$

$$\frac{\partial f}{\partial z_0} = (z_0 - z_i)[(x_i - x_0)^2 + (y_i - y_0)^2 + (z_i - z_0)^2]^{-1/2}$$

(One could also take the derivative with respect to the velocity v—in which case there would be n = 5 unknowns—and hence attempt to find corrections to the starting velocity.) Thus a system of m linear equations is constructed from which an attempt is made to find the difference or gradient vector, $\vec{dx}$, between the improved solution, $\vec{x}_0$, and the approximate solution, $\vec{x}_0'$

$$d_i[v(t_i - t_0) - d_i] = d_i v\Delta t + (x_0 - x_i)\Delta x + (y_0 - y_i)\Delta y + (z_0 - z_i)\Delta z, \qquad \text{(A-8)}$$

where $\Delta t_0 = t_0 - t_0'$, $\Delta x_0 = x_0 - x_0'$, $\Delta y_0 = y_0 - y_0'$, $\Delta z_0 = z_0 - z_0'$.

When $\vec{dx}_0$ is found, it is then added to $\vec{x}_0'$ yielding the improved solution $\vec{x}_0$. This improved solution $\vec{x}_0'$ then becomes a new $\vec{x}_0'$ from which a new gradient vector is found and so on iteratively until the gradient vector is essentially zero. At this point $\vec{x}_0'$ and $\vec{x}_0$ are essentially equal, a local minimum of equation 1 has been found, and the microseismic source is at t_0, x_0, y_0, z_0.

SPATIAL-GRADIENT BASIS

The derivation of the spatial-gradient basis function follows that given in Lienert (*16*). Here equation 1 is first rewritten as a function of the travel-time residuals

$$t_i - t_0 - T_i(x,y,z) = \Delta t_0 + \Delta x_0 \frac{\partial T_i}{\partial x} + \Delta y_0 \frac{\partial T_i}{\partial y} + \Delta z_0 \frac{\partial T_i}{\partial z},$$

where T_i (x, y, z) are the calculated travel times from the source to the *i*th receiver. Since the source location and the source origin time are interrelated through equation 1, the full-gradient vector can be decomposed into two separate gradients: one is three-dimensional—the spatial gradient—and increments the estimate of the source location; the other is one-dimensional and increments the estimate of the source origin time using the solution of each spatial gradient. The one-dimensional gradient is

$$t_0 + \Delta t_0 = \langle t_i \rangle - \langle T_i \rangle - \Delta x_0 \left\langle \frac{\partial T_i}{\partial x} \right\rangle - \Delta y_0 \left\langle \frac{\partial T_i}{\partial y} \right\rangle - \Delta z_0 \left\langle \frac{\partial T_i}{\partial z} \right\rangle, \qquad \text{(A-9)}$$

where the brackets, < >, represent weighted means in general. This equation is used to get an update of the estimate of the origin time, i.e., $t_0 + \Delta t_0$, for each increment of the spatial gradient, i.e., $(\Delta x_0, \Delta y_0, \Delta z_0)$. The basis function for the spatial gradient is

$$t_i - \langle t_i \rangle = \left(\frac{\partial T_i}{\partial x} - \left\langle \frac{\partial T_i}{\partial x} \right\rangle \right) \Delta x_0 + \left(\frac{\partial T_i}{\partial y} - \left\langle \frac{\partial T_i}{\partial y} \right\rangle \right) \Delta y_0 + \left(\frac{\partial T_i}{\partial z} - \left\langle \frac{\partial T_i}{\partial z} \right\rangle \right) \Delta z_0 \qquad \text{(A-10)}$$

where n = 3 since the unknowns involve only the corrections to the spatial coordinates of the source.

In practice, the magnitude of the gradient vector for either gradient basis can be limited to some specified maximum size. Thus, if $|\vec{dx}_0| > \max$, one finds a new $\vec{dx}_0'$ such that $|\vec{dx}_0'| = \max$ and $\vec{dx}_0'$ is parallel to $\vec{dx}_0$. This helps stabilize convergence in cases of marginal convergence by not overshooting the local minimum. In cases of divergence (as when the source is far outside of the receiver array), limiting the gradient vector can allow one to get an estimate of the direction of the source relative to the initial starting point by tracking the path of all of the approximate solutions $\vec{x}_0'$ (away from the array). For stope arrays with characteristic dimensions of about 100 m, a good maximum to the magnitude of the gradient vector is about 3 m. (Note that this is not the most efficient method of reaching the minimum; see Press, (*13*), Section 14.4 for improved strategies such as the Levenberg-Marquardt method.)

APPENDIX B.—SUBSETS OF DIRECT BASIS FUNCTIONS

Each of the above direct basis functions can be used to form a system with more than m equations. Whether or not the full system or a subset of the system of equations can be used depends on the weighting of each basis function.

SW-GBM BASIS SUBSETS

Each nonzero SW-GBM basis function involves information from two different receivers, j and k. (If the indices j and k are interchanged in equation A-1, the same equation is formed.) Therefore, the set of all possible SW-GBM equations can be referenced by specifying all possible pairs of j and k. As an example, let m = 5:

1	2	3	4	5
1	2			
1		3		
1			4	
1				5
	2	3		
	2		4	
	2			5
		3	4	
		3		5
			4	5

It is easy to see that there are m(m-1)/2 different pairings since an even permutation of the indices kl results in the same equation (A-1) and an odd permutation results in only a sign change of the equation A-1. The m(m-1)/2 equations, however, are not necessarily independent. It is also fairly easy to see that a subset of as few as m-1 independent equations can be selected as long as all of the information is weighted equally. For example,

1	2	3	4	5
1	2			
1		3		
1			4	
1				5

1	2	3	4	5
1	2			
	2	3		
		3	4	
			4	5

represent two different subsets of m-1 independent equations which can be used in linear combination to form all the other (m-1)(m/2 - 1) equations (assuming equal weighting). Suppose that the ordering of the receiver indices in the above example indicates the order in which signals arrived at the receivers (positive arrival-time ordering). Then the first m-1 subset above represents that suggested by Salamon and Wiebols (*11*), and the second m-1 subset above represents that suggested by Godson (*12*). Notice that the first subset drastically overemphasizes the information from receiver 1; imagine the results if the receiver coordinates and/or the arrival-time pick of receiver 1 are significantly in error! Note that these two cases are not the only choices of m-1 independent equations; for example,

1	2	3	4	5
1	2			
1		3		
		3	4	
			4	5

1	2	3	4	5
1	2			
	2	3		
	2		4	
			4	5

represent only two more of the many different possible subsets of m-1 independent equations that can be selected.

A subset like that suggested by Godson results in a set of equations that are information poor for two receivers. This can be altered by always including an equation for that receiver pair, making m equations:

1	2	3	4	5
1	2			
	2	3		
		3	4	
			4	5
1				5

For such subsets, one equation can always be formed by a linear combination of the other m-1 equations, but the representation of information from each receiver is balanced.

So far, this discussion has assumed that all the information for the m receivers has equal weight, i.e., all arrival times and all station coordinates have the same relative uncertainties—or at least there are no criteria by which to assign different weights. If, however, different weights, w_{jk} are given to each basis function A-1 (i.e., the weighted basis function is w_{jk} (A-1)), then, in general, there could be as many as m(m-1)/2 independent SW-GBM basis functions. Here w_{jk} represents some weighting function for the information for receiver j combined with the information for receiver k.

By using different subsets of the SW-GBM basis function, it is easy to see that there is a staggering number of different possible source location solutions that could be obtained. If all the basis functions are weighted independently, resulting in m(m-1)/2 independent basis equations, then there are

$$\sum_{r=4}^{m(m-1)/2} \left[\begin{matrix} m(m-1)/2 \\ r \end{matrix} \right], \qquad \text{(B-1)}$$

where $\left[\begin{matrix} n \\ r \end{matrix} \right] = \frac{n!}{r!(n-r)!} = \frac{n(n-1)\ (n-2)\ldots(n-r+1)}{r!}$,

possible different solutions.

This subset problem leads to a vast number of potential source location solutions. For m = 4 and equal weighting, a three-dimensional location cannot be attempted since only three equations can be formed and there are four unknowns. For m = 4 and unequal weighting, six independent equations can be formed from which 15 subsets can be formed using four equations, six subsets using five equations, and the total set of six equations; thus 22 different source locations would be possible. For m = 5 and equal weighting, a unique three-dimensional source location is obtained. For m = 5 and unequal weighting and using all possible different subsets of 4, 5, 6, 7, 8, 9, and 10 equations, there are, in general, 848 different possible source locations!

BLD BASIS SUBSETS

Each nonzero BLD basis function involves information from three different receivers, say, j, k, and l. Therefore, the set of all possible BLD equations can be referenced by specifying all possible triplets of j, k, and l. Again, let m = 5:

1	2	3	4	5
1	2	3		
1	2		4	
1	2			5
1		3	4	
1		3		5
1			4	5
	2	3	4	
	2	3		5
	2		4	5
		3	4	5

It is easy to see that there are at least m(m-1)(m-2)/6 different triplets. Since it is obvious from equation A-6 that interchanging the indices j and k results in only a sign change of the equation, it may be thought at first that there could be as many as m(m-1)(m-2)/2 different equations depending on the choice of l. Fortunately, this turns out not to be the case: the indices j, k, and l are all interchangeable; an even permutation of the indices jkl results in the same equation A-6, an odd permutation results in only a sign change of the equation A-6. So in the above example of m = 5, the 10 different combinations for j, k, and l give all the possible different equations A-6 to within a sign change, regardless of which index is selected for j, k, or l.

The subset of m-2 equations suggested by Blake (*9*) could be indicated by the following for m = 5:

1	2	3	4	5
1	2	3		
1	2		4	
1	2			5 ,

where, for this subset of Blake's, the ordering of the receiver indices indicates the order in which signals arrived at the receivers (again, positive arrival-time ordering). This type of subset of the BLD basis function, like the Salamon and Wiebol subset of the SW-GBM basis function, over-emphasizes information for some receivers. Here, the information of the first and second hit receivers is overemphasized in the final solution.

A better subset of m-2 equations might be something like

1	2	3	4	5
1	2	3		
	2	3	4	
		3	4	5

with or without arrival-time ordering. A balanced subset of m equations might be something like

1	2	3	4	5
1	2			5
1	2	3		
	2	3	4	
		3	4	5
1			4	5

with or without arrival-time ordering.

LINEAR DEPENDENCE OF DIRECT BASIS FUNCTIONS

The question arises as to whether or not any of the above subsets of the BLD basis function represents a basis of independent equations from which the rest of the m(m-1)(m-2)/6 equations can be formed. The answer is no, even for the case of equal information weighting.

For equally weighted SW-GBM basis functions, two equations of different jk indices can be selected to form a third SW-GBM equation as long as one index is repeated. For example, equation $(A\text{-}1)_{12} + (A\text{-}1)_{23} = (A\text{-}1)_{13}$ with $w_{12} = w_{23} = w_{13}$, noting that $(A\text{-}1)_{23} = -(A\text{-}1)_{32}$. Thus, for equal weighting, either the Salamon and Wiebols m-1 subset or the Godson m-1 subset gives a basis subset from which the other equations can be formed.

For equally weighted BLD basis functions, three equations of different jkl indices can be selected to form a fourth BLD equation as long as one index is repeated in all three equations and the other indices are repeated in two of the three equations. For example, equation $(A\text{-}6)_{123} + (A\text{-}6)_{214} + (A\text{-}6)_{134} = (A\text{-}6)_{234}$ with $w_{123} = w_{124} = w_{134} = w_{234}$, noting that $(A\text{-}6)_{214} = -(A\text{-}6)_{124}$. Thus, for the BLD basis, there are at least (m-1)(m-2)/2 independent equations (more if weighting is unequal), with a maximum of

all m(m-1)(m-2)/6 equations being independent if all have different weights. Thus for m = 4 and equal weighting, there are (m-1)(m-2)/2 = three independent equations from which to form the m(m-1)(m-2)/6 = four equations of the full system. For m = 5 and equal weighting, there are six independent equations; for example,

1	2	3	4	5
1	2	3		
1	2		4	
1	2			5
1		3	4	
1		3		5
1			4	5

represents one possible selection.

By using different subsets of the BLD basis function, the number of different possible source locations is even larger than with the SW-GBM basis. If all the BLD basis functions are weighted independently, resulting in m(m-1)(m-2)/6 independent basis equations, then there are in general

$$\sum_{r=3}^{m(m-1)(m-2)/6} \left[\begin{matrix} m(m-1)(m-2)/6 \\ r \end{matrix} \right],$$

possible different solutions.

APPENDIX C.—EXAMPLES OF SOURCE LOCATION PROCESS

Explicit numerical examples of the source location process are given for (1) the SW-GBM basis function with the m-1 time-ordered GBM subset, (2) the spatial-gradient basis function, and (3) the full-gradient function. Selected for this numerical example is one of the calibration blasts discussed in the text which had the following set of observed arrival time readings, P(obs), for each corresponding station whose coordinates are given in meters:

station	P(obs)(s)	x (m)	y (m)	z (m)
r2	0.04508	3438.534	2793.316	-364.462
r3	.04506	3421.774	2816.882	-346.750
r4.1	.04162	3400.516	2803.324	-363.934
r5	.04368	3417.924	2778.723	-364.260
r15	.05730	3464.037	2856.791	-418.682
r7	.04526	3384.110	2815.730	-363.047
r8	.05114	3354.194	2816.320	-363.709
r9.1	.04316	3416.935	2816.420	-362.691
r10	.05878	3414.929	2746.971	-272.683
r12	.04732	3440.619	2767.520	-363.983

The arrival time readings have a precision of ±0.00002 s and the coordinates have a precision of ±0.005 m. The P-wave velocity is assumed to be a constant 5.020 km/s.

The set of linear equations formed by the SW-GBM basis function (appendix A) with the m-1 time-ordered GBM subset (appendix B) is given below. Here, all weighting for individual stations coordinates and arrival-time readings are equal (i.e., unity). The solution x has been found using the QR (hence, "least-squares") algorithm described in the text which employees partial pivoting. The units used for this example are meters for distance, milliseconds for time, and meters per millisecond (equals kilometers per second) for velocity. Since there are m = 10 arrival-time readings, 9 equations are formed. See below. The source is located (using this set of equations) to be at x_0 = 3,412.9 m, y_0 = 2,798.6 m, and z_0 = -362.7 m. The origin time is directly computed to be 0.03777 seconds (relative to the same time origin as the arrival-time readings).

The SW-GBM solution does not, in general, yield a very good direct estimate of the origin time of the source. In this example with the origin time at 0.03777 s, the travel-time residuals are computed to be

station	P(calc)	P(o-c)
r2	0.042999	0.002081
r3	.042909	.002151
r4.1	.040424	.001196
r5	.041876	.001804
r7	.044444	.000816
r8	.049989	.001151
r9.1	.041405	.001755
r10	.058446	.000334
r12	.046078	.001242
r15	.056811	.000489

where P(o-c) is the difference between the observed and calculated arrival times, (P(calc)), for the P-wave, i.e., the P-wave travel-time residuals. The effective rms of the travel-time residuals is 0.001435 s normalized by 1/m, or 0.001853 s normalized by 1/(m-4), where 4 is the effective number of unknowns in the problem (origin time and three spatial coordinates). However, the origin time can be computed independently from the estimate of the source coordinates and the observed arrival times at each receiver; for this example, the mean of the values for the origin time (A-7) yields a revised estimate of the origin time of the source to be 0.039074738 s, with the revised travel-time residuals to be

station	P(calc)	P(o-c)
r2	0.044301	0.000779
r3	.044211	.000849
r4.1	.041725	-0.000105
r5	.043178	.000502
r7	.045746	-.000486
r8	.051291	-.000151
r9.1	.042707	.000453
r10	.059748	-.000968
r12	.047380	-.000060
r15	.058113	-.000813

The effective rms of the travel-time residuals is now reduced to 0.000605 s normalized by 1/m, or 0.000781 s normalized by 1/(m-4).

$$A = \begin{bmatrix} -77.617088 & 32.837891 & 26.191895 & 2.485962 \\ -26.208632 & 1.978027 & -75.394043 & -3.138000 \\ -69.552963 & 7.699707 & 76.318359 & 35.020020 \\ -1.008039 & 33.520020 & -47.132324 & -35.424011 \\ -9.072160 & -108.847656 & 44.828125 & 2.830017 \\ -103.825714 & 113.017578 & -96.419922 & -1.872009 \\ -192.530853 & -172.849609 & 97.600098 & 0.547974 \\ -310.469116 & 219.686035 & 80.941895 & -109.945984 \\ -74.592972 & -98.216309 & -219.640137 & 291.997986 \end{bmatrix} \quad b = \begin{bmatrix} 181337.859375 \\ -204157.828125 \\ 224319.671875 \\ -4680.454102 \\ -247032.125000 \\ 112363.328125 \\ -324426.406250 \\ 1004708.000000 \\ -1058486.750000 \end{bmatrix} \quad x = \begin{bmatrix} 37.772820 \\ 3412.905762 \\ 2798.638184 \\ -362.666046 \end{bmatrix}$$

The location based on the spatial-gradient basis function (appendix A) is now computed. By way of illustration, the starting point for the iterative process is selected to be the revised SW-GMB solution from above (t_0 = 0.039074738 s, x_0 = 3412.905762 m, y_0 = 2798.638184 m, and z_0 = -362.666046 m), though almost any starting point in or around the receiver array could have been selected as a starting point. For the first iteration, the linear system Ax = b is set up and solved, by the QR algorithm:

$$A = \begin{bmatrix} -0.189479 & 0.060893 & 0.025504 & 0.778861 \\ -.063410 & -.120467 & -.111098 & .849044 \\ .190580 & -.049664 & .030849 & -.105471 \\ -.043424 & .213069 & .027282 & .501761 \\ -.101470 & -.100726 & .128624 & -.812930 \\ .176394 & -.081186 & .014134 & -.485710 \\ .195818 & -.036953 & .015256 & -.150945 \\ -.038918 & -.173794 & .012140 & .453275 \\ .001221 & .119656 & -.160850 & -.968294 \\ -.127313 & .169171 & .018160 & -.059605 \end{bmatrix} \quad b = \begin{bmatrix} \\ \\ \\ \\ -.812930 \\ \\ \\ \\ \\ \end{bmatrix}$$

with

$$x = \begin{bmatrix} -1.857610 \\ -.756399 \\ -.598912 \end{bmatrix}$$

The solution vector x indicates the *change* in the estimate of spatial coordinates of the source. The first correction to the origin-time estimate is obtained independently via equation (A-9) and is found to be -0.000032 s. After making the corrections to the source origin time and coordinates, 10 new equations are formed using the spatial-gradient basis function and solved iteratively until the corrections to the source coordinates are sufficiently small (approaching zero). The final iteration of the spatial-gradient basis function for this example gave a solution of t_0 = 0.039026 s, x_0 = 3410.91 m, y_0 = 2797.77 m, and z_0 = -363.41 m. This solution yields the following travel-time residuals:

station	P(calc)	P(o-c)
r2	0.044603	0.000477
r3	.044520	.000540
r4.1	.041377	.000243
r5	.043074	.000606
r7	.045454	-.000194
r8	.050914	.000226
r9.1	.042932	.000228
r10	.059755	-.000975
r12	.047473	-.000153
r15	.058299	-.000999

Thus for the spatial-gradient basis function, the effective rms of the travel-time residuals is reduced to 0.000553 s normalized by 1/m, or 0.000714 s normalized by 1/(m-4).

The final solution for the full-gradient basis function (appendix A) yields a solution of t_0 = 0.038555 s, x_0 = 3414.46 m, y_0 = 2800.86 m, and z_0 = -359.70 m, giving the following travel-time residuals:

station	P(calc)	P(o-c)
r2	0.043668	0.001412
r3	.042910	.002150
r4.1	.041500	.000120
r5	.043109	.000571
r7	.045322	-.000062
r8	.050976	.000164
r9.1	.041750	.001410
r10	.058944	-.000164
r12	.047039	-.000281
r15	.057521	-.000221

Thus for the full-gradient basis function, the effective rms of the travel-time residuals is 0.000955 s normalized by 1/m, or 0.001233 s normalized by 1/(m-4).

☆ U.S. GPO: 1991—611-016/48,846